Hindawi Publishing Corporation
Modelling and Simulation in Engineering
Volume 2012, Article ID 756508, 16 pages
doi:10.1155/2012/756508

Research Article

A Three-Dimensional Geometry-Based Statistical Model of 2×2 Dual-Polarized MIMO Mobile-to-Mobile Wideband Channels

Jun Chen and Thomas G. Pratt

Department of Electrical Engineering, University of Notre Dame, Notre Dame, IN 46556, USA

Correspondence should be addressed to Thomas G. Pratt, tpratt@nd.edu

Received 27 April 2012; Accepted 27 July 2012

Academic Editor: Carlos A. Gutierrez

A three-dimensional (3D) model for wide-band dual-polarized (DP) multiple-input-multiple-output (MIMO) mobile-to-mobile (M2M) channels is proposed. Using geometrical scattering based on concentric spheres at the transmitter (Tx) and at the receiver (Rx), a 3D parametric reference model for 2×2 M2M DP multipath fading channels is developed. The channel model assumes the use of colocated half-wavelength dipole antennas for vertical and horizontal polarizations at both transmit and receive stations. Model parameters include the velocities of the Tx and Rx nodes, the distance between the nodes, the 3D antenna pattern gains, the azimuth and elevation angles of arrival and departure, the geometrical distribution of the scatterers, the Rician K-factors defining the fading envelope distributions, the maximum Doppler frequency, the scattering loss factors, the cross-polar power discrimination ratio (XPD), and the copolarization power ratio (CPR). Using the proposed model, expressions for joint time-frequency correlation functions (TFCFs) are derived which are used to investigate system behavior over different wide sense stationary uncorrelated scattering (WSSUS) channel realizations. The numerical results illustrate the sensitivities of the TFCF to simultaneous time and frequency offsets for the 2×2 DP-MIMO architectures.

1. Introduction

For nearly two decades, multiple-input-multiple-output (MIMO) communications systems [1–3] have been rigorously studied, leading to the adoption of MIMO in a number of wireless communications standards such as Long Term Evolution (LTE) and 802.11n. The LTE provides high-speed wireless communications for mobile phones and data terminals, while 802.11n supports MIMO, frame aggregation, and security improvements for wireless local area networks (WLAN). In these systems, multiple antennas can be used at both the transmitter (Tx) and receiver (Rx) to exploit the diversity and channel capacity afforded by MIMO architectures. In array-based MIMO systems, CP antennas at mobile stations and access points are ideally separated by at least one-half wavelength and at cellular base stations by at least ten wavelengths to achieve significant diversity or multiplexing gains [4]. In space-constrained implementations such as with handheld devices, use of antenna spacings less than one-half wavelength can lead to antenna correlations that lend themselves to beamforming gains, but ohmic coupling effects can deplete any gains that would otherwise be achieved with these strategies [5]. An alternative architecture for space-constrained deployments involves the use of dual-polarized (DP) antennas. This strategy has the advantage of offering colocated antennas that provide largely uncorrelated fading responses, although usually with asymmetrical average powers among the MIMO channel matrix entries. Hence, the channel behaviors for DP systems are substantively different from conventional copolarized (CP) channels, the latter which exhibit similar average powers. The relative performance of DP-MIMO in comparison to traditional MIMO with CP arrays will be dictated by the disparities in these responses. While DP architectures are receiving increasing attention, they have thus far been studied with much less rigor than CP systems.

To characterize DP systems, especially in wideband signaling applications, modeling of dispersive input-to-output polarimetric channel behavior is important. Many

theoretical models [6–11] provide statistical representations of polarimetric channels based on cross-polarization coupling (XPC), but do not characterize polarization-frequency behavior that is needed to represent wider-band, frequency-selective channels for the analysis of DP communications systems. For example, XPC is most often analyzed in the narrowband sense and yet it has been shown that the XPC can vary with frequency. It also exhibits correlation in the frequency dimension in a manner that depends on the channel's temporal dispersion properties and polarization coupling [12]. Statistical channel models in literature that address time-selective and frequency-selective behavior often assume that the time dispersion (due to time delays) and the frequency dispersion (due to Doppler spread) are statistically independent, where the time delays depend on the relative locations of the random scatterers and the Doppler spreads depend on the motion of the Tx and Rx antennas [13, 14]. However, this assumption is broken if both the time delays and the Doppler spreads depend on the relative location of the random scatterers (e.g., the angles of departure and the angles of arrivals). Because these phenomena would not be expected to be statistically independent, it is of interest to examine joint correlation functions in time and frequency, which is an application of the model that we consider in our paper.

Analytical approaches such as Kronecker or eigenbeam models have also been used for model simulations, and these have dealt with narrowband channels. An analytical framework based on a Kronecker model is presented in [15] to model narrowband DP Rayleigh and Rician fading channels for arbitrary array sizes. The framework uses a relatively small number of physical parameters to analyze the benefits of multiple polarization architectures. In other work, a 3D polarized narrowband spatial channel model is presented in [7], and the impact of elevation angle on capacity is reported in [16]. These models assume ideal dipole antennas and unity cross-polar discrimination ratios.

Another approach to characterize channels for DP systems involves the use of geometric scattering models. Geometrical scattering models [17–19] have the advantage that they are able to represent important channel behaviors, including mutual effects that arise from polarization coupling, time-dispersion, angle-dispersion, and frequency-dispersion. However, they also are more complex. Early two-dimensional (2D) geometric scattering models were developed for narrowband CP single-input single-output (SISO) mobile-to-mobile (M2M) Rayleigh fading channels [20–22]. In [23], the polarisation-sensitive geometric modelling is developed with a direction-of-arrival (DOA) distribution that depends on the polarisation states of the transmitting antennas, the receiving antennas and the polarisation properties of the scatterers. These models were 2D in the sense that the models treated electromagnetic propagation only in a fixed-elevation plane and did not model elevation antenna pattern dependencies or distributions of scatterers in the elevation dimension.

Some three-dimensional (3D) models have been proposed to overcome shortcomings of 2D M2M channel models, particularly in environments where deployed antenna heights are lower than surrounding buildings and obstacles. In [18], a 3D wideband M2M mathematical reference model was proposed based on a concentric-cylinders geometry using a superposition of line-of-sight (LOS), single bounce at the transmit side (SBT), single bounce at the receive side (SBR), and double-bounce (DB) rays in a variety of urban environments. The analysis approach proved useful to characterize M2 M correlations, but to date has only been applied to the analysis of CP MIMO channels with unity-gain idealized dipole antennas. Recently, a 3D polarized channel model has been proposed to treat spatially-separated orthogonally polarized elements [19]. The model deals exclusively with the double-bounce ray and narrowband channels.

In this paper, we develop a 3D geometric scattering model for 2×2 M2M DP wideband channels based on concentric spheres to evaluate joint time frequency correlation functions associated with the subchannel fading envelopes. The use of concentric spheres is motivated by the ease with which scatterer locations may be identified for a given radius, azimuth AOD, and elevation AOD, and by its capability to support the modeling of overhead reflectors. The DP-MIMO channel is constructed assuming a DP antenna at both the Tx and the Rx, where the polarization basis at the Rx is matched to the polarization basis used at the Tx. The received signals can be translated to an arbitrary orthogonally-polarized basis by applying a unitary transformation to the received signal vectors [24] without impacting theoretical performance measures such as capacity and diversity.

We assume a channel with wide sense stationary uncorrelated scattering (WSSUS) where the channel correlation function is invariant over time, and the scatterers with different path delays are uncorrelated [25, 26]. Channel transfer functions for each transmit antenna/receive antenna pair are derived as a superposition of LOS, SBT, SBR, and DB component rays. The transfer functions are used to form time-frequency correlation functions (TFCF) for the assumed 3D nonisotropic scattering environment, where scattering distributions are characterized in the azimuth dimension through the von Mises distribution and in the elevation dimension by a cosine distribution. The 3D scattering propagation model used to evaluated the TFCFs simulates the effects of the antenna pattern gains, the geometrical distribution of scatterers and the associated azimuth/elevation angles of arrival and departure, the K-factor of the fading distributions, the maximum Doppler frequency, the scattering loss factors, the cross-polar discrimination (XPD), and the copolarization ratio (CPR).

The remainder of the paper is organized as follows. The 3D DP 2×2 MIMO M2M model is presented in Section 2. In Section 3, we derive transfer functions and TFCFs for each subchannel of the DP-MIMO channel and for each ray path type for 3D nonisotropic scattering environments. Numerical results of the joint correlation functions associated with the 2×2 DP channel models are presented in Section 4. We conclude with a summary of our findings in Section 5.

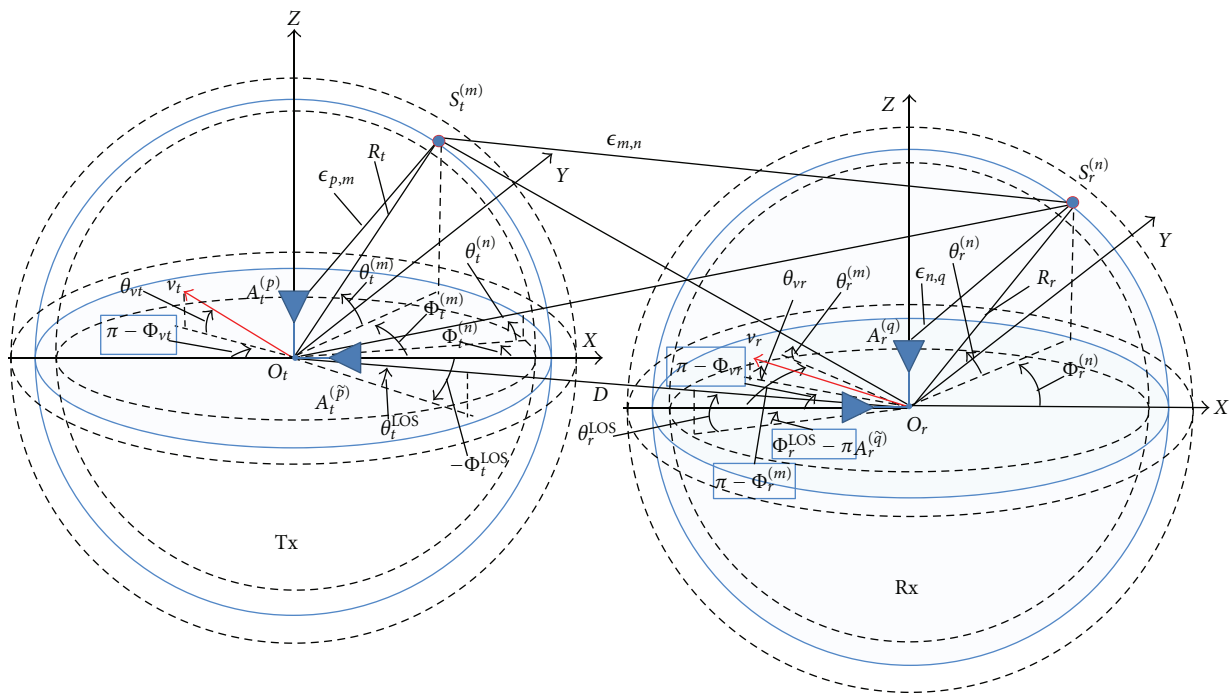

Figure 1: Concentric-spheres for 3D colocated DP channel model. The signals from the Tx antennas arrive in parallel at the Rx antenna array.

2. 2×2 DP-MIMO Channel Model Based on Concentric Spheres

The concentric sphere geometry-based scattering model assumes a mobile Tx and a mobile Rx, both equipped with DP antennas using a matched polarization basis. Radio propagation between the Tx and the Rx is characterized by 3D WSSUS under channels that can include line-of-sight (LOS) and non-line-of-sight (NLOS) components, where scattering centers in the latter case reside on concentric spheres about either the Tx, the Rx, or both. The linearly time-variant MIMO channel can be represented by a 2×2 impulse response matrix in terms of time t and delay τ

$$\mathbf{H}(t,\tau) = \begin{bmatrix} h_{qp}(t,\tau) & h_{q\tilde{p}}(t,\tau) \\ h_{\tilde{q}p}(t,\tau) & h_{\tilde{q}\tilde{p}}(t,\tau) \end{bmatrix}. \quad (1)$$

Figure 1 illustrates the concentric sphere model for a MIMO M2M channel with DP antennas. One DP antenna with vertically-polarized and horizontally-polarized components denoted by $A_t^{(p)}$ and $A_t^{(\tilde{p})}$, respectively, is located at the center of the Tx sphere (O_t). A second DP antenna with corresponding components denoted by $A_r^{(q)}$ and $A_r^{(\tilde{q})}$ is located at the center of the Rx sphere (O_r). At the Tx, M fixed scatterers reside within the volume of a sphere defined by a radius R_t. The mth transmit scatterer is denoted by $S_t^{(m)}$, where $1 \le m \le M$ and resides on the surface of a sphere with radius R_m, where $R_m < R_t$. Similarly at the Rx, N scatterers occupy the spherical volume with a radius R_r. The nth receive scatterer is denoted by $S_r^{(n)}$, where $1 \le n \le N$ and resides on the surface of a sphere with radius R_n, where $R_n < R_r$. The set of scatterers is comprised of H scatterers (reflecting horizontally polarized waves) and V scatterers (reflecting vertical polarized waves). We assume that the distribution of the H scatterers and the V scatterers are identical and that the number of scatterers for each are the same, although this may not be true in general.

The center of the Tx sphere serves as the global origin of a rectangular coordinate system. At time $t = 0$, the Rx is a distance D from the Tx with XYZ coordinates denoted by $(\Delta_x, \Delta_y, \Delta_z)$. The height difference between the Tx and the Rx antennas is included in the offset Δ_z. The symbols $\epsilon_{p,m}$, $\epsilon_{m,q}$, $\epsilon_{p,n}$, $\epsilon_{n,q}$, $\epsilon_{m,n}$ and $\epsilon_{p,q}$ denote distances $d(A_t^{(p)}, S_t^{(m)})$, $d(S_t^{(m)}, A_r^{(q)})$, $d(A_t^{(p)}, S_r^{(n)})$, $d(S_r^{(n)}, A_r^{(q)})$, $d(S_t^{(m)}, S_r^{(n)})$, and $d(A_t^{(p)}, A_r^{(q)})$, respectively, where $d(\cdot)$ denotes the distance between the two coordinates. The symbols $\theta_t^{(m)}, \theta_t^{(n)}$ are the elevation angles of departure (EAoD, relative to the XY plane) to the scatterers $S_t^{(m)}$ and $S_r^{(n)}$, respectively, whereas $\phi_t^{(m)}, \phi_t^{(n)}$ are the azimuth angles of departure (AAoD, in the XY plane relative to the Z-axis) to the scatterers $S_t^{(m)}$ and $S_r^{(n)}$ respectively. Similarly, the symbols $\theta_r^{(m)}, \theta_r^{(n)}$ denote the elevation angles of arrival (EAoA, relative to the x-y plane) reflected from the scatterers $S_t^{(m)}$ and $S_r^{(n)}$, respectively, whereas $\phi_r^{(m)}, \phi_r^{(n)}$ denote the azimuth angles of arrival (AAoA, in the XY plane relative to the z-axis) reflected from the scatterers $S_t^{(m)}$ and $S_r^{(n)}$ respectively. For the LOS component between the Tx and the Rx, the symbols θ_t^{LOS} and ϕ_t^{LOS} are the elevation angle of departure (relative to the XY plane) and the azimuth angle of departure in the XY plane relative to the Z-axis, respectively. Similarly, the symbols θ_r^{LOS}

and ϕ_r^{LOS} are the elevation angle of arrival and the azimuth angle of arrival, respectively. The Tx and Rx are moving with speeds v_t and v_r in directions described by the elevation angles θ_{vt} and θ_{vr} relative to the XY plane, respectively, and by the azimuth angles ϕ_{vt} and ϕ_{vr} in the XY plane, respectively.

2.1. Scatterer Distributions. The directions of scatterers are described by azimuth and elevation angle distributions. Several different distributions, such as uniform, Gaussian, Laplacian, and von Mises, have been used in the literature to characterize the azimuth angles of departure and arrival. von Mises Fisher (VMF) distributions are effective to model both AAoD and AAoA for spatial fading correlation models [27] and have the advantage that the probability density function approximates many of distributions and admits closed-form solutions [18]. To simplify the modeling, it is assumed that the azimuth and elevation angles are independent, enabling the use of a product of distribution functions instead of a joint distribution. The scatterer distributions are synthesized using different angle distributions for the azimuth and the elevation dimensions. The Von Mises Fisher probability density function (pdf) distribution is used for azimuth dimensions, including for angles of departure ($\phi_t^{(m)}$ and $\phi_r^{(n)}$) and angles of arrival ($\phi_t^{(n)}$ and $\phi_r^{(m)}$). The von Mises pdf is defined as [28]

$$f(\phi) = \frac{\exp[\kappa\cos(\phi-\mu)]}{2\pi I_0(\kappa)}, \quad \phi \in [-\pi,\pi), \tag{2}$$

where $\mu \in [-\pi,\pi)$ is the mean value of the scatterer directions in the azimuth plane, κ controls the spread of scatterers around the mean μ, and $I_0(\cdot)$ is the zero-order modified Bessel function of the first kind. When $\kappa = 0$, $f(\phi)=1/2\pi$ is a uniform distribution, corresponding to isotropic scattering in azimuth. As κ increases, the scatterers become more clustered about the mean angle μ, and scattering is nonisotropic.

The random elevation angles of departure and arrival can be characterized by a uniform, cosine or Gaussian distribution. In [18, 29], a cosine pdf is used as it may fit with the typical propagation in M2M communications, where the Tx and Rx are in motion and equipped with low elevation antennas. A cosine distribution employed for the elevation angles of departure and arrival is given by [29]:

$$f(\theta) = \begin{cases} \dfrac{\pi}{4|\theta_{\max}|}\cos\left(\dfrac{\pi}{2}\dfrac{\theta}{\theta_{\max}}\right), & |\theta| \le |\theta_{\max}| \le \dfrac{\pi}{2}, \\ 0, & \text{otherwise.} \end{cases} \tag{3}$$

where $\theta_{\max}$ is the maximum elevation angle which we assume to have a value near 20°. This maximum elevation angle is typical of M2M wireless communications where both the Tx and Rx are equipped with low elevation antennas.

The above-mentioned distributions are used to represent the response from a cluster, which describes a group of scatterers located within an isolated solid angle, and the response from multiple clusters compose the aggregate response from the channel. In [27], a mixture of Von Mises distributions is proposed for modeling the 3D direction of scatterers in the presence of multiple clusters of scatterers over the propagation channel. Mathematically, each distribution in the mixture of M VMFs at the Tx or N VMFs at the Rx can be described as $f(\phi_t^{(m)}|\overline{\phi}_t^{(m)},\kappa_m)(1 \le m \le M)$ or $f(\phi_r^{(n)}|\overline{\phi}_r^{(n)},\kappa_n)(1 \le n \le N)$. Note that $\overline{\phi}_t^{(m)}$ or $\overline{\phi}_r^{(n)}$ is the mean azimuth angle of the mth or nth cluster; κ_m or κ_n is the concentration of the mth or nth cluster. Hence, the overall density functions of the mixture model consisting of M VMF distributions for the cluster azimuth angles $\phi_t^{(m)}$ at the transmitter and N VMF distributions for the cluster azimuth angles $\phi_r^{(n)}$ at the Rx can be described as [27]

$$\begin{aligned} \overline{f}(\phi_t) &= \sum_{m=1}^{M} \nu_m\left(f\phi_t^{(m)} \mid \overline{\phi}_t^{(m)},\kappa_m\right), \\ \overline{f}(\phi_r) &= \sum_{n=1}^{N} \nu_n\left(f\phi_r^{(n)} \mid \overline{\phi}_r^{(n)},\kappa_n\right), \end{aligned} \tag{4}$$

where M and N the number of clusters at the Tx and Rx, respectively; ν_m or ν_n is defined as the *a priori* probability that mth or nth cluster was generated. Similarly, the overall density functions of the mixture model consisting of the cosine distributions for the elevation angles $\theta_t^{(m)}$ at the Tx and $\theta_r^{(n)}$ at the Rx can be expressed as

$$\begin{aligned} \overline{f}(\theta_t) &= \sum_{m=1}^{M} \nu_m\left(\theta_t^{(m)} \mid f\overline{\theta}_t^{(m)}\right), \\ \overline{f}(\theta_r) &= \sum_{n=1}^{N} \nu_n\left(\theta_r^{(n)} \mid \overline{\theta}_r^{(n)}\right), \end{aligned} \tag{5}$$

where $\overline{\theta}_t^{(m)}$ and $\overline{\theta}_r^{(n)}$ are the mean elevation angle of the mth or nth cluster at the Tx and Rx, respectively.

Signals from the Tx antenna elements that propagate directly to the Rx antenna elements form the LOS component. Signals reflected exclusively from the scatterers located around the Tx before arriving at the Rx antenna elements are collectively called the SBT component. Similarly, transmit signals reflected only by scatterers located around the Rx before arriving at the Rx antenna elements form the SBR component. The DB component is formed from the signals that are reflected from scatterers about both the Tx and the Rx before arriving at the Rx antenna elements. For each realization of the WSSUS channel, the channel impulse responses and TFCFs can be written as superpositions of the LOS, SBT, SBR, and DB signal components.

The channel impulse responses for the subchannels $A_t^{(p)} \to A_r^{(q)} \to, A_t^{(\tilde{p})} \to A_r^{(q)}, A_t^{(p)} \to A_r^{(\tilde{q})}$ and $A_t^{(\tilde{p})} \to A_r^{(\tilde{q})}$ can be written as a superposition of the LOS, SBT, SBR and DB signals,

$$h_{ab}(t,\tau) = h_{ab}^{\mathrm{SBR}}(t,\tau) + h_{ab}^{\mathrm{SBR}}(t,\tau) + h_{ab}^{\mathrm{DB}}(t,\tau) + h_{ab}^{\mathrm{LOS}}(t,\tau), \tag{6}$$

where the $h^{l}_{ab}(t,\tau)(a \in \{p,\tilde{p}\}, b \in \{q,\tilde{q}\}, l \in \{\text{LOS, SBT, SBR, DB}\})$ represent the impulse response functions between antenna elements a and b along the l path respectively, and $h_{ab}(t,\tau)$ represents the total response between antenna elements a and b.

2.2. Single Bounce Channel Impulse Response. The time varying impulse responses of the single-bounce components are given by

$$\begin{aligned} h^{\text{SBT}}_{\text{ab}}(t,\tau) =& \sqrt{\frac{\eta_{t,pq}}{K+1}}\frac{1}{\sqrt{N}}\sum_{n=1}^{M}\xi_{a,n,b}g_{a,n,b}(t) \\ &\times \delta(\tau-\tau_{a,m,b}) \\ &\times \left[\sqrt{G^{(v)}_{a}\left(\phi^{(m)}_{t},\theta^{(m)}_{t}\right)}\ \sqrt{G^{(h)}_{a}\left(\phi^{(m)}_{t},\theta^{(m)}_{t}\right)}\right] \\ &\times \begin{bmatrix} 1 & \sqrt{r^{(m)}_{p\tilde{q}}} \\ \sqrt{r^{(m)}_{\tilde{p}q}} & 1 \end{bmatrix}\begin{bmatrix} \sqrt{G^{(v)}_{b}\left(\phi^{(m)}_{r},\theta^{(m)}_{r}\right)} \\ \sqrt{G^{(h)}_{b}\left(\phi^{(m)}_{r},\theta^{(m)}_{r}\right)} \end{bmatrix} \\ &\times \exp\left(j\phi^{(m)}_{ab}\right)\rho^{\text{SBT}}_{m}, \\ h^{\text{SBR}}_{ab}(t,\tau) =& \sqrt{\frac{\eta_{t,pq}}{K+1}}\frac{1}{\sqrt{N}}\sum_{n=1}^{M}\xi_{a,n,b}g_{a,n,b}(t) \\ &\times \delta(\tau-\tau_{a,n,b}) \\ &\times \left[\sqrt{G^{(v)}_{a}\left(\phi^{(n)}_{t},\theta^{(n)}_{t}\right)}\ \sqrt{G^{(h)}_{a}\left(\phi^{(n)}_{t},\theta^{(n)}_{t}\right)}\right] \\ &\times \begin{bmatrix} 1 & \sqrt{r^{(n)}_{p\tilde{q}}} \\ \sqrt{r^{(n)}_{\tilde{p}q}} & 1 \end{bmatrix}\begin{bmatrix} \sqrt{G^{(v)}_{b}\left(\phi^{(n)}_{r},\theta^{(n)}_{r}\right)} \\ \sqrt{G^{(h)}_{b}\left(\phi^{(n)}_{r},\theta^{(n)}_{r}\right)} \end{bmatrix} \\ &\times \exp\left(j\phi^{(n)}_{ab}\right)\rho^{\text{SBR}}_{n}, \end{aligned} \tag{7}$$

where the parameter K is the Rician K factor which is a ratio of the power through the LOS path relative to the power through the scattered paths. The power ratio coefficients $\eta_{t,ab}$ and $\eta_{r,ab}$ $(a \in \{p,\tilde{p}\}, b \in \{q,\tilde{q}\})$ in (7) specify the fraction of the power of the single-bounce components along the subchannels $A^{(a)}_{t} \rightarrow A^{(b)}_{r}$ with respect to the average transmit power P_{ab} between the Tx antenna element a and the Rx antenna element b. The relationships among these, and related power ratio coefficients are shown in (29). $\xi_{a,m,b}$ and $\xi_{a,n,b}$ denote the signal amplitudes and $\tau_{a,m,b}$ and $\tau_{a,n,b}$ denote time delays of the multipath components propagating from antenna element a to antenna element b via transmit scatterer m and from antenna element a to antenna element b via receive scatterer n $(a \in \{p,\tilde{p}\}, b \in \{q,\tilde{q}\})$, respectively.

$G^{(v)}_{a}(\cdot,\cdot)$, $G^{(h)}_{a}(\cdot,\cdot)$, $G^{(v)}_{b}(\cdot,\cdot)$, and $G^{(h)}_{b}(\cdot,\cdot)$ $(a \in \{p,\tilde{p}\}, b \in \{q,\tilde{q}\})$ denote the antenna patterns of the pth, $\tilde{p}$th, qth, and $\tilde{q}$th antenna element with vertical(v) or horizontal(h) polarizations, respectively. We assume that a half-wavelength dipole is used for each element where the spherical coordinate system defining antenna orientations are illustrated in Figure 2. The antenna feed is situated at

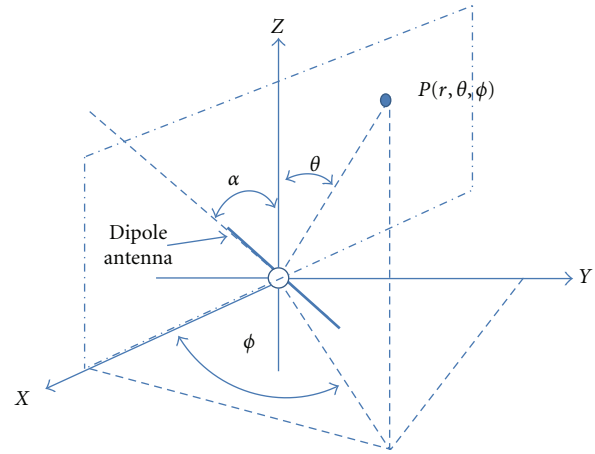

Figure 2: Half-wavelength dipole antenna and its coordinate system.

the origin of the coordinate system and the antenna elements are inclined at the angle α from the Z axis in the vertical ZX plane. A thin dipole is assumed and the element radius is ignored. The radiation power gain patterns of the half-wavelength dipole for vertical and horizontal polarizations are given by [30]

$$\begin{aligned} G^{(v)}(\theta,\phi) &= 1.641(\cos\theta\cos\phi\sin\alpha - \sin\theta\cos\alpha)^{2}\frac{\cos^{2}(\pi\zeta/2)}{(1-\zeta^{2})^{2}}, \\ G^{(h)}(\theta,\phi) &= 1.641\sin^{2}\phi\sin^{2}\alpha\frac{\cos^{2}(\pi\zeta/2)}{(1-\zeta^{2})^{2}}, \end{aligned} \tag{8}$$

where

$$\zeta = \sin\theta\cos\phi\sin\alpha + \cos\theta\cos\alpha. \tag{9}$$

For illustration, antenna gain patterns of the half-wavelength dipole with inclination angles of 0 and $\pi/2$ are shown in Figures 3 and 4 respectively.

$\tau_{a,m,b}$ and $\tau_{a,n,b}$ denote time delays of the multipath components propagating from antenna element $A^{(a)}_{t}$ to antenna element $A^{(b)}_{r}$ via the scatterer $S^{(m)}_{t}$ and from antenna element $A^{(a)}_{t}$ to antenna element $A^{(b)}_{r}$ via the scatterer $S^{(n)}_{r}$, respectively. $g_{a,m,b}(t)$ and $g_{a,n,b}(t)$ are the time-varying phase functions along the path $A^{(a)}_{t} \rightarrow S^{(m)}_{t} \rightarrow A^{(b)}_{r}$ and $a \rightarrow S^{(n)}_{r} \rightarrow b$, respectively. Since the antenna elements are collocated and share a common phase center, the time delays $\tau_{a,m,b}$ or $\tau_{a,n,b}$ are equivalent between antennas elements $A^{(a)}_{t}$ and $A^{(b)}_{r}$, that is,

$$\begin{aligned} \tau_{p,m,q} &= \tau_{p,m,\tilde{q}} = \tau_{\tilde{p},m,q} = \tau_{\tilde{p},m,\tilde{q}}, \\ \tau_{p,n,q} &= \tau_{p,n,\tilde{q}} = \tau_{\tilde{p},n,q} = \tau_{\tilde{p},n,\tilde{q}}. \end{aligned} \tag{10}$$

Similarly, $g_{a,m,b}(t)$ and $g_{a,n,b}(t)$ satisfy

$$\begin{aligned} g_{p,m,q}(t) &= g_{p,m,\tilde{q}}(t) = g_{\tilde{p},m,q}(t) = g_{\tilde{p},m,\tilde{q}}(t), \\ g_{p,n,q}(t) &= g_{p,n,\tilde{q}}(t) = g_{\tilde{p},n,q}(t) = g_{\tilde{p},n,\tilde{q}}(t). \end{aligned} \tag{11}$$

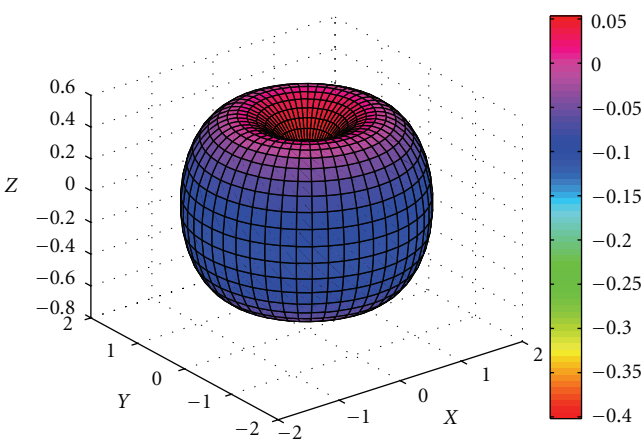

Figure 3: Gain patterns of half-wavelength dipole antenna with inclination angle of 0: $G^{(v)}(\theta,\phi)$. The horizontal component $G^{(h)}(\theta,\phi)$ is zero.

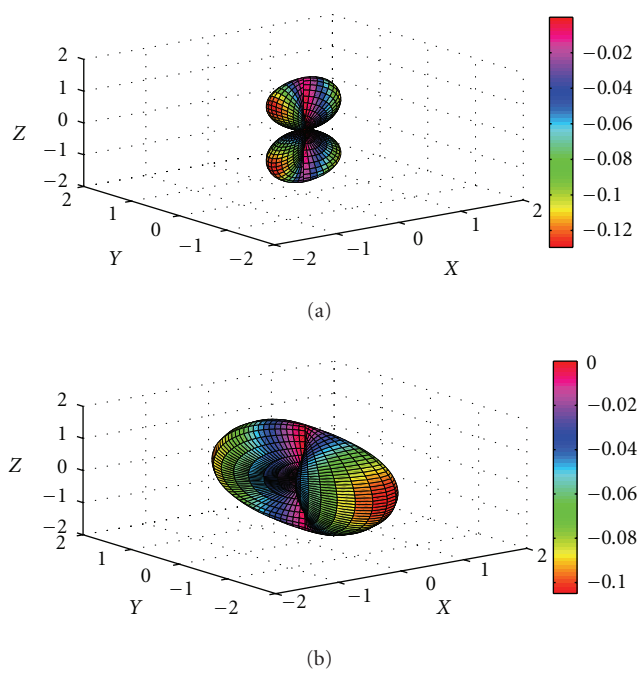

Figure 4: Gain patterns of half-wavelength dipole antenna with inclination angle of $\pi/2$: (a) $G^{(v)}(\theta,\phi)$, and (b) $G^{(h)}(\theta,\phi)$.

The random variable $\phi_{ab}^{(m)}$ represents the uniformly-distributed random phase offset associated with the path to each scatterer $S_t^{(m)}$ between the V or H component of the Tx antenna elements and the V or H component of the Rx antenna elements. Similarly, the random variable $\phi_{ab}^{(n)}$ is the uniformly-distributed phase offset associated with the path to each scatterer $S_r^{(n)}$ between the V or H component of the Tx antenna elements and the V or H component of the Rx antenna elements.

$r_{\tilde{p}q}^{(m)}$, $r_{p\tilde{q}}^{(n)}$, $r_{\tilde{p}q}^{(n)}$, and $r_{\tilde{p}q}^{(n)}$ represent the inverse of the channel cross-polar discrimination ratios along the single bounce path to scatterer m or scatterer n, and have statistical means that follow

$$E\left\{r_{p\tilde{q}}^{(m)}\right\} = E\left\{r_{p\tilde{q}}^{(n)}\right\} = \frac{1}{\mathrm{XPD}_p},$$
$$E\left\{r_{\tilde{p}q}^{(m)}\right\} = E\left\{r_{\tilde{p}q}^{(n)}\right\} = \frac{1}{\mathrm{XPD}_{\tilde{p}}}. \tag{12}$$

Here, the channel cross-polar discrimination for each transmit polarization is defined as

$$\mathrm{XPD}_p = \frac{E\left|h_{qp}\right|^2}{E\left\{\left|h_{\tilde{q}p}\right|^2\right\}},$$
$$\mathrm{XPD}_{\tilde{p}} = \frac{E\left\{\left|h_{\tilde{q}\tilde{p}}\right|^2\right\}}{E\left\{\left|h_{\tilde{q}\tilde{p}}\right|^2\right\}}, \tag{13}$$

where $E\{\cdot\}$ denotes the expectation operator.

The XPD depends on channel parameters and the environment, such as the distance between the Tx and the Rx, the angles of arrival and departure (both azimuth and elevation), the delay spread of the multipath components, and the transmit and receive antenna polarization basis.

We define a parameter $\mathrm{CPR}_{qp\tilde{q}\tilde{p}}$ as the copolar power ratio between the average powers transmitted through the vertical-vertical subchannel and the average powers transmitted through the horizontal-horizontal subchannel:

$$\mathrm{CPR}_{qp,\tilde{q}\tilde{p}} = \frac{E\left\{\left|h_{\tilde{q}\tilde{p}}\right|^2\right\}}{E\left\{\left|h_{\tilde{q}\tilde{p}}\right|^2\right\}}. \tag{14}$$

The CPR depends on the Brewster angle phenomenon [31].

The XPD and CPR, when expressed in decibel (dB), are often observed as having the normal distribution with $N(\mu,\sigma)$. In [7], the mean of XPD varies from 0 to 18 dB, with the standard deviation in order of 3 $\sim$ 8 dB. Normally, the received power in the vertical-to-vertical transmission is reported to be greater than that in the horizontal-to-horizontal transmission (CPR $>$ 0 dB). For example, the mean of the CPR is reported to vary between 0 and 6 dB [15]. Depending on the propagation environment and transmission configuration, the CPR may be less than 0 dB when the amplitude of vertically polarized waves is degraded more than that of horizontally polarized waves or the transmission power of horizontally polarized waves is greater than that of vertically polarized waves. When the XPD or

CPR in dB is denoted as X, the expectations in (12) can be computed as

$$E\left\{\sqrt{r_{p\tilde{q}}^{(m)}}\right\} = E\left\{\sqrt{r_{\tilde{p}q}^{(m)}}\right\} = E\left\{10^{-(X/20)}\right\},$$
$$E\left\{\sqrt{\frac{1}{\mathrm{CPR}_{qp,\tilde{q}\tilde{p}}}}\right\} = E\left\{10^{-(X/20)}\right\}. \tag{15}$$

When X has the normal distribution with $N(\mu,\sigma)$, then the expectation $E\{10^{-X/20}\}$ over an interval $[x_1, x_2]$ can be expressed as

$$E\left\{10^{-(X/20)}\right\} = \int_{x_1}^{x_2} 10^{-(x/20)} \frac{1}{\sqrt{2\pi\sigma^2}} \exp\left(-\frac{(x-\mu)^2}{2\sigma^2}\right) dx. \tag{16}$$

For simplicity, we adopt the normal XPD model to characterize cross-polarized components in the 3D modeling of 2×2 DP-MIMO M2M channels.

When the elevation angles of arrival/departure are small, the distances $d(A_t^{(p)}, S_t^{(m)})$, $d(S_t^{(m)}, A_r^{(q)})$, $d(A_t^{(p)}, S_r^{(n)})$, $d(S_r^{(n)}, A_r^{(q)})$, $d(S_t^{(m)}, S_r^{(n)})$ and $d(A_t^{(p)}, A_r^{(q)})$ can be approximated as below

$$\begin{aligned}
\left|d\left(A_t^{(p)}, S_t^{(m)}\right)\right| &= \epsilon_{p,m} \approx R_t,\\
\left|d\left(S_t^{(m)}, A_r^{(q)}\right)\right| &= \epsilon_{m,q} \approx D,\\
\left|d\left(A_t^{(p)}, S_r^{(n)}\right)\right| &= \epsilon_{p,n} \approx D,\\
\left|d\left(S_r^{(n)}, A_r^{(q)}\right)\right| &= \epsilon_{n,q} \approx R_r,\\
\left|d\left(A_t^{(p)}, A_r^{(q)}\right)\right| &= \epsilon_{pq} \approx D,\\
\left|d\left(S_t^{(m)}, S_r^{(n)}\right)\right| &= \epsilon_{m,n} \approx \sqrt{(R_t - R_r)^2 + D^2}.
\end{aligned} \tag{17}$$

Furthermore, using the Taylor series expansion, the amplitudes of the multipath components, $\xi_{p,m,q}$ or $\xi_{p,m,\tilde{q}}$ is approximately given by

$$\begin{aligned}
\xi_{p,m,q} &= \xi_{p,m,\tilde{q}}\\
&= \left[\left|d\left(A_t^{(p)}, S_t^{(m)}\right)\right| + \left|d\left(S_t^{(m)}, A_r^{(q)}\right)\right|\right]^{-\gamma/2}\\
&\approx A_m\left(1 - \frac{\gamma}{2}\frac{R_t}{D}\right),
\end{aligned} \tag{18}$$

where γ is the path loss exponent, whose value is normally in the range of 2 to 4, depending upon the propagation environment. $\xi_{\tilde{p},m,\tilde{q}}$ or $\xi_{\tilde{p},m,q}$ is approximated as

$$\begin{aligned}
\xi_{\tilde{p},m,\tilde{q}} &= \xi_{\tilde{p},m,q}\\
&= \sqrt{\frac{1}{\mathrm{CPR}_{qp,\tilde{q}\tilde{p}}}}\left[\left|d\left(A_t^{(p)}, S_t^{(m)}\right)\right| + \left|d\left(S_t^{(m)}, A_r^{(q)}\right)\right|\right]^{-\gamma/2}\\
&\approx A_m\sqrt{\frac{1}{\mathrm{CPR}_{qp,\tilde{q}\tilde{p}}}}\left(1 - \frac{\gamma}{2}\frac{R_t}{D}\right),
\end{aligned} \tag{19}$$

where A_m is defined as

$$A_m = D^{-\gamma/2}. \tag{20}$$

Similarly, $\xi_{p,n,q}$ or $\xi_{p,n,\tilde{q}}$ is approximated as

$$\begin{aligned}
\xi_{p,n,q} &= \xi_{p,n,\tilde{q}}\\
&= \left[\left|d\left(A_r^{(p)}, S_r^{(n)}\right)\right| + \left|d\left(S_r^{(n)}, A_r^{(q)}\right)\right|\right]^{-\gamma/2}\\
&\approx A_m\left(1 - \frac{\gamma}{2}\frac{R_r}{D}\right),
\end{aligned} \tag{21}$$

$\xi_{\tilde{p},n,\tilde{q}}$ or $\xi_{\tilde{p},n,q}$ is approximated as

$$\begin{aligned}
\xi_{\tilde{p},n,\tilde{q}} &= \xi_{\tilde{p},n,q}\\
&= \sqrt{\frac{1}{\mathrm{CPR}_{qp,\tilde{q}\tilde{p}}}}\left[\left|d\left(A_r^{(p)}, S_r^{(n)}\right)\right| + \left|d\left(S_r^{(n)}, A_r^{(q)}\right)\right|\right]^{-\gamma/2}\\
&\approx A_m\sqrt{\frac{1}{\mathrm{CPR}_{qp,\tilde{q}\tilde{p}}}}\left(1 - \frac{\gamma}{2}\frac{R_r}{D}\right).
\end{aligned} \tag{22}$$

The time delays $\tau_{p,m,q}$ and $\tau_{p,n,q}$ are the travel times of the signals scattered from the Tx scatterer $S_t^{(m)}$, and from the Rx scatterer $S_r^{(n)}$, respectively

$$\tau_{p,m,q} = \frac{\epsilon_{p,m} + \epsilon_{m,q}}{c}, \tag{23}$$

$$\tau_{p,n,p} = \frac{\epsilon_{p,n} + \epsilon_{n,q}}{c}, \tag{24}$$

where c is the speed of the light.

The time-varying phase function $g_{a,m,b}(t)$ along the path $A_t^{(p)} \to S_t^{(m)} \to A_r^{(q)}$ is given by

$$\begin{aligned}
g_{p,m,q}(t) = {} & \exp\left[-j\frac{2\pi}{\lambda_c}\left(\epsilon_{p,m} + \epsilon_{m,q}\right)\right]\\
&\times\exp\left[j2\pi t f_{t\max}\cos\left(\phi_t^{(m)} - \phi_{vt}\right)\cos\theta_t^{(m)}\cos\theta_{vt}\right]\\
&\times\exp\left(j2\pi t f_{t\max}\sin\theta_t^{(m)}\sin\theta_{vt}\right)\\
&\times\exp\left[j2\pi t f_{r\max}\cos\left(\phi_r^{(m)} - \phi_{vr}\right)\cos\theta_r^{(m)}\cos\theta_{vr}\right]\\
&\times\exp\left(j2\pi t f_{r\max}\sin\theta_r^{(m)}\sin\theta_{vr}\right),
\end{aligned} \tag{25}$$

where $f_{t\max} = vt/\lambda_c$ and $f_{r\max} = vr/\lambda_c$ are the maximum.

Doppler frequencies associated with the Tx and Rx respectively and λ_c denotes the carrier wavelength.

The time-varying phase function $g_{p,m,b}(t)$ along the path $A_t^{(p)} \to S_r^{(n)} \to A_r^{(q)}$ is given by

$$\begin{aligned} g_{p,n,q}(t) = {} & \exp\left[-j\frac{2\pi}{\lambda_c}\left(\epsilon_{p,n}+\epsilon_{n,q}\right)\right] \\ & \times\exp\left[j2\pi t f_{t\max}\cos\left(\phi_t^{(n)}-\phi_{vt}\right)\cos\theta_t^{(n)}\cos\theta_{vt}\right] \\ & \times\exp\left(j2\pi t f_{t\max}\sin\theta_t^{(n)}\sin\theta_{vt}\right) \\ & \times\exp\left[j2\pi t f_{r\max}\cos\left(\phi_r^{(n)}-\phi_{vr}\right)\cos\theta_r^{(n)}\cos\theta_{vr}\right] \\ & \times\exp\left(j2\pi t f_{r\max}\sin\theta_r^{(n)}\sin\theta_{vr}\right). \end{aligned} \tag{26}$$

The parameters ρ_m^{SBT} and ρ_n^{SBR} represent scattering loss factors, and are governed by [32]

$$\rho = \exp\left[-8\left(\frac{\pi\sigma_h\sin\theta_i}{\lambda_c}\right)^2\right]I_0\left[8\left(\frac{\pi\sigma_h\sin\theta_i}{\lambda_c}\right)^2\right], \tag{27}$$

where σ_h is the standard deviation of the surface height of the scatterer, θ_i is a given angle of incidence, and $I_0(\cdot)$ is the zero-order modified Bessel function of the first kind.

2.3. Double-Bounce Channel Impulse Response. The double-bounce components of the channel impulse responses are

$$\begin{aligned} & h_{pq}^{\mathrm{DB}}(t,\tau) \\ & = \sqrt{\frac{\eta_{tr,pq}}{K+1}}\frac{1}{\sqrt{MN}}\sum_{m=1}^{M}\sum_{n=1}^{N}\xi_{a,m,n,b}g_{a,m,n,b}(t) \\ & \quad\times\delta\left(\tau-\tau_{a,m,n,b}\right) \\ & \quad\times\left[\sqrt{G_a^{(v)}\left(\phi_t^{(m)},\theta_t^{(m)}\right)}\sqrt{G_a^{(h)}\left(\phi_t^{(m)},\theta_t^{(m)}\right)}\right] \\ & \quad\times\begin{bmatrix}1 & \sqrt{r_{p\tilde{q}}^{(m)}}\\ \sqrt{r_{\tilde{p}q}^{(m)}} & 1\end{bmatrix}\begin{bmatrix}1 & \sqrt{r_{p\tilde{q}}^{(n)}}\\ \sqrt{r_{\tilde{p}q}^{(n)}} & 1\end{bmatrix} \\ & \quad\times\begin{bmatrix}\sqrt{G_b^{(v)}\left(\phi_r^{(n)},\theta_r^{(n)}\right)}\\ \sqrt{G_b^{(h)}\left(\phi_r^{(n)},\theta_r^{(n)}\right)}\end{bmatrix} \\ & \quad\times\exp\left(j\phi_{ab}^{(m,n)}\right)\rho_m^{\mathrm{SBT}}\rho_n^{\mathrm{SBR}}, \end{aligned} \tag{28}$$

where the power ratio coefficients $\eta_{tr,ab}$ $(a \in \{p,\tilde{p}\}, b \in \{q,\tilde{q}\})$ in (28), specify the ratio of the power of the double-bounce ray along the subchannels $A_t^{(a)} \to A_r^{(b)}$ with respect to the averaged transmit power P_{ab} between the Tx antenna element a and the Rx antenna element b. The power ratio coefficients of the single-bounce and the double-bounce rays satisfy

$$\eta_{t,ab}+\eta_{r,ab}+\eta_{tr,ab} = 1, \quad (a \in \{p,\tilde{p}\}, b \in \{q,\tilde{q}\}). \tag{29}$$

$\xi_{a,m,n,b}$ denotes the amplitude and $\tau_{a,m,n,b}$ denotes the time delay of the multipath components along the path $A_t^{(a)} \to S_t^{(m)} \to S_r^{(n)} \to A_r^{(b)}$ $(a \in \{p,\tilde{p}\}, b \in \{q,\tilde{q}\})$. The amplitudes of the multipath components $\xi_{p,m,n,q}$ and $\xi_{p,m,n,\tilde{q}}$ are given by

$$\begin{aligned} \xi_{p,m,n,q} = {} & \xi_{p,m,n,\tilde{q}} \\ & \times\left[\left|d\left(A_t^{(p)},S_t^{(m)}\right)\right|+\left|d\left(S_t^{(m)},S_r^{(n)}\right)\right| \right. \\ & \left. +\left|d\left(S_r^{(n)},A_r^{(q)}\right)\right|\right]^{-\gamma/2} \\ \approx {} & A_m\left(1-\frac{\gamma}{2}\frac{R_t+R_r}{D}\right). \end{aligned} \tag{30}$$

The amplitudes of the multipath components $\xi_{\tilde{p},m,n,\tilde{q}}$ and $\xi_{\tilde{p},m,n,q}$ are given by

$$\begin{aligned} \xi_{\tilde{p},m,n,\tilde{q}} = {} & \xi_{\tilde{p},m,n,q} = \sqrt{\frac{1}{\mathrm{CPR}_{qp,\tilde{q}\tilde{p}}}} \\ & \times\left[\left|d\left(A_t^{(p)},S_t^{(m)}\right)\right|+\left|d\left(S_t^{(m)},S_r^{(n)}\right)\right| \right. \\ & \left. +\left|d\left(S_r^{(n)},A_r^{(q)}\right)\right|\right]^{-\gamma/2} \\ \approx {} & A_m\sqrt{\frac{1}{\mathrm{CPR}_{qp,\tilde{q}\tilde{p}}}}\left(1-\frac{\gamma}{2}\frac{R_t+R_r}{D}\right). \end{aligned} \tag{31}$$

As DP antenna pair are colocated at the center of Tx and the center of Rx without considering the size of antennas, the time delays $\tau_{a,m,n,b}$ are equivalent between antennas $A_t^{(a)}$ and $A_r^{(b)}$

$$\tau_{p,m,n,q} = \tau_{p,m,n,\tilde{q}} = \tau_{\tilde{p},m,n,q} = \tau_{\tilde{p},m,n,\tilde{q}}. \tag{32}$$

The time delay $\tau_{p,m,n,q}$ is the travel time of the signals scattered from both the Tx scatterer $S_t^{(m)}$ and the Rx scatterer $S_r^{(n)}$

$$\tau_{p,m,n,q} = \frac{\epsilon_{p,m}+\epsilon_{m,n}+\epsilon_{n,q}}{c}. \tag{33}$$

Similarly, $g_{a,m,n,b}(t)$ satisfy

$$g_{p,m,n,q}(t) = g_{p,m,n,\tilde{q}}(t) = g_{\tilde{p},m,n,q}(t) = g_{\tilde{p},m,n,\tilde{q}}(t). \tag{34}$$

The time-varying function $g_{p,m,n,q}(t)$ is given by

$$\begin{aligned} g_{p,m,n,q}(t) = {} & \exp\left[-j\frac{2\pi}{\lambda_c}\left(\epsilon_{p,m}+\epsilon_{m,n}+\epsilon_{n,q}\right)\right] \\ & \times\exp\left[j2\pi t f_{t\max}\cos\left(\phi_t^{(m)}-\phi_{vt}\right)\cos\theta_t^{(m)}\cos\theta_{vt}\right] \\ & \times\exp\left(j2\pi t f_{t\max}\sin\theta_t^{(m)}\sin\theta_{vt}\right) \\ & \times\exp\left[j2\pi t f_{r\max}\cos\left(\phi_r^{(n)}-\phi_{vr}\right)\cos\theta_r^{(n)}\cos\theta_{vr}\right] \\ & \times\exp\left(j2\pi t f_{r\max}\sin\theta_r^{(n)}\sin\theta_{vr}\right). \end{aligned} \tag{35}$$

The random variable $\phi_{ab}^{(m,n)}$ is the phase offset of the double-bounce path scattered by both the Tx scatterer $S_t^{(m)}$ and the Rx scatterer $S_r^{(n)}$ between the V or H component of the Tx antenna elements and the V or H component of the Rx antenna elements.

2.4. LOS Channel Impulse Response. The LOS components of channel impulse responses are

$$h_{ab}^{\mathrm{LOS}}(t,\tau) = \sqrt{\frac{K}{K+1}}\xi_{a,b}^{\mathrm{LOS}} g_{a,b}^{\mathrm{LOS}}(t)\delta\left(\tau - \tau_{a,b}^{\mathrm{LOS}}\right) \times \sqrt{G_a\left(\phi_t^{\mathrm{LOS}},\theta_t^{\mathrm{LOS}}\right)G_b\left(\phi_r^{\mathrm{LOS}},\theta_r^{\mathrm{LOS}}\right)}, \tag{36}$$

where $\xi_{a,b}^{\mathrm{LOS}}$ ($a \in \{p,\tilde{p}\}$, $b \in \{q,\tilde{q}\}$) denotes the amplitude and $\tau_{a,b}^{\mathrm{LOS}}$ denotes the time delay of the LOS components between the antenna element $A_t^{(a)}$ at the Tx and the antenna element $A_r^{(b)}$ at the Rx. The time-varying function $g_{a,b}^{\mathrm{LOS}}(t)$ is defined as

$$\begin{aligned} g_{p,q}^{\mathrm{LOS}}(t) &= g_{p,\tilde{q}}^{\mathrm{LOS}}(t) = g_{\tilde{p},q}^{\mathrm{LOS}}(t) = g_{\tilde{p},\tilde{q}}^{\mathrm{LOS}}(t) \\ &= \exp\left(-j\frac{2\pi}{\lambda_c}\epsilon_{p,q}\right) \\ &\quad \times \exp\left[j2\pi t f_{t\max}\cos\left(\phi_t^{\mathrm{LOS}} - \phi_{vt}\right)\cos\theta_t^{\mathrm{LOS}}\cos\theta_{vt}\right] \\ &\quad \times \exp\left(j2\pi t f_{t\max}\sin\theta_t^{\mathrm{LOS}}\sin\theta_{vt}\right) \\ &\quad \times \exp\left[j2\pi t f_{r\max}\cos\left(\phi_r^{\mathrm{LOS}} - \phi_{vr}\right)\cos\theta_r^{\mathrm{LOS}}\cos\theta_{vr}\right] \\ &\quad \times \exp\left(j2\pi t f_{r\max}\sin\theta_r^{\mathrm{LOS}}\sin\theta_{vr}\right). \end{aligned} \tag{37}$$

The amplitude of the LOS components $\xi_{a,b}^{\mathrm{LOS}}$ is given by

$$\begin{aligned} \xi_{p,q}^{\mathrm{LOS}} &= \xi_{p,\tilde{q}}^{\mathrm{LOS}} \approx D^{-\frac{\gamma}{2}} = A_m, \\ \xi_{\tilde{p},\tilde{q}}^{\mathrm{LOS}} &= \xi_{\tilde{p},q}^{\mathrm{LOS}} \approx \sqrt{\frac{1}{\mathrm{CPR}_{qp,\tilde{q}\tilde{p}}}}D^{-\frac{\gamma}{2}} = A_m\sqrt{\frac{1}{\mathrm{CPR}_{qp,\tilde{q}\tilde{p}}}}. \end{aligned} \tag{38}$$

The time delay $\tau_{a,b}^{\mathrm{LOS}}$ is the travel time of the signal from the Tx antenna element $A_t^{(a)}$ and the Rx antenna element $A_r^{(b)}$. Consider the following:

$$\tau_{p,q}^{\mathrm{LOS}} = \tau_{p,\tilde{q}}^{\mathrm{LOS}} = \tau_{\tilde{p},q}^{\mathrm{LOS}} = \tau_{\tilde{p},\tilde{q}}^{\mathrm{LOS}} = \frac{\epsilon_{p,q}}{c}. \tag{39}$$

It is assumed that the elevation angles (θ_t^{LOS}, θ_r^{LOS}, $\theta_t^{(m)}$, $\theta_t^{(n)}$, $\theta_r^{(m)}$, and $\theta_r^{(n)}$) and the azimuth angles (ϕ_t^{LOS}, ϕ_r^{LOS}, $\phi_t^{(m)}$, $\phi_t^{(n)}$, $\phi_r^{(m)}$ and $\phi_r^{(n)}$) are independent random variables. The radii R_t of the Tx sphere and R_r of the Rx sphere are also independent. The phase offsets $\phi_{ab}^{(m)}$, $\phi_{ab}^{(n)}$, and $\phi_{ab}^{(m,n)}$ are assumed to be uniformly random variables on the interval $[-\pi,\pi)$ that are independent from the elevation angles, azimuth angles, and radii of the scattering spheres. Using the Central Limit Theorem [33, 34], we posit that the delay-spread functions $h_{ab}^{\mathrm{SBT}}(t,\tau)$, $h_{ab}^{\mathrm{SBR}}(t,\tau)$, $h_{ab}^{\mathrm{LOS}}(t,\tau)$, and $h_{ab}^{\mathrm{DB}}(t,\tau)$ are zero-mean complex Gaussian random processes.

2.5. Time-Variant Transfer Functions. The time-variant transfer function is the Fourier transform of the channel impulse response with respect to the delay τ. Consider the following:

$$\mathbf{T}_{ab}(t,f) = F_\tau\{h_{ab}(t,\tau)\} = \mathbf{T}_{ab}^{\mathrm{SBT}}(t,f) + \mathbf{T}_{ab}^{\mathrm{SBR}}(t,f) + \mathbf{T}_{ab}^{\mathrm{DB}}(t,f) + \mathbf{T}_{ab}^{\mathrm{LOS}}(t,f), \tag{40}$$

where $\mathbf{T}_{ab}^{\mathrm{SBT}}(t,f)$, $\mathbf{T}_{ab}^{\mathrm{SBR}}(t,f)$, $\mathbf{T}_{ab}^{\mathrm{DB}}(t,f)$, and $\mathbf{T}_{ab}^{\mathrm{LOS}}(t,f)$ ($a \in \{p,\tilde{p}\}, b \in \{q,\tilde{q}\}$) are time-variant transfer functions for the SBT, SBR, DB and LOS components, respectively.

3. Polarization Matched Time-Frequency Correlation Functions

Wide-sense stationarity and uncorrelated scatterers are often assumed to be valid for mobile radio channels [18]. In this paper, time and frequency dispersion are modeled dependently over a wide sense stationary uncorrelated scattering channel for a 3D nonisotropic scattering environment. For such channels, the time-frequency correlation function is an effective way of characterizing the statistical dependencies in the temporal and frequency domains associated with the mobile-to-mobile channels. Since the polarization states of antennas at both the Tx and Rx are matched, we derive the matched polarization-basis time-frequency correlation function to show the relationship between the frequency and the time of the 3D statistical model for 2×2 DP antennas.

For a WSSUS channel, the TFCF of the time-varying transfer function $\mathbf{T}_{ab}$ ($a \in \{p,\tilde{p}\}, b \in \{q,\tilde{q}\}$) is defined in terms of the time difference Δ_t and the frequency separation Δ_f

$$\rho_{ab}\left(\Delta_t,\Delta_f\right) = E\left[\mathbf{T}_{ab}(t,f)^*\mathbf{T}_{ab}\left(t+\Delta_t, f+\Delta_f\right)\right], \tag{41}$$

where $a \in \{p,\tilde{p}\}, b \in \{q,\tilde{q}\}$ and p, $\tilde{p}$, q, $\tilde{q}$ correspond to vertical and horizontal antenna polarizations. $E[\cdot]$ is the expectation operator, and $*$ denotes the complex conjugate operation. The TFCFs in (41) can be rewritten as the superposition of the TFCFs of the SBT, SBR, DB and LOS components. Consider

$$\rho_{ab}\left(\Delta_t,\Delta_f\right) = \rho_{ab}^{\mathrm{SBT}}\left(\Delta_t,\Delta_f\right) + \rho_{ab}^{\mathrm{SBR}}\left(\Delta_t,\Delta_f\right) + \rho_{ab}^{\mathrm{DB}}\left(\Delta_t,\Delta_f\right) + \rho_{ab}^{\mathrm{LOS}}\left(\Delta_t,\Delta_f\right). \tag{42}$$

In order to estimate the time frequency correlations, we make the assumption that the number of scatterers in the 3D reference model is infinite so that the discrete azimuth angles ($\phi_t^{(m)}$, $\phi_r^{(m)}$, $\phi_t^{(n)}$ and $\phi_r^{(n)}$), the discrete elevation angles ($\theta_t^{(m)}$, $\theta_r^{(m)}$, $\theta_t^{(n)}$, and $\theta_r^{(n)}$) and the radii R_t, R_r can be represented as continuous random variables with probability density functions of $f(\phi_r^{(s)})$, $f(\phi_t^{(s)})$, $f(\theta_r^{(s)})$, $f(\theta_t^{(s)})$, $f(R_t)$, and $f(R_r)$, respectively. The form of these pdf's are as follows.

The Tx azimuth angles are characterized by the von Mises pdf in (2) as

$$f\left(\phi_t^{(S)}\right) = \frac{\exp\left[\kappa_t^{(S)}\cos\left(\phi_t^{(S)} - \mu_t^{(S)}\right)\right]}{2\pi I_0\left(\kappa_t^{(S)}\right)}, \tag{43}$$

where $\mu_t^{(S)} \in [-\pi, \pi)$ is the mean value of angle at which the Tx scatterers are distributed in the x-y plane and $\kappa_t^{(S)}$ controls the spread of Tx scatterers around the mean $\mu_t^{(S)}$. Similarly, the Rx azimuth angles are characterized by

$$f\left(\phi_r^{(S)}\right) = \frac{\exp\left[\kappa_r^{(S)}\cos\left(\phi_r^{(S)} - \mu_r^{(S)}\right)\right]}{2\pi I_0\left(\kappa_r^{(S)}\right)}, \tag{44}$$

where $\mu_r^{(S)} \in [-\pi, \pi)$ is the mean value of angle at which the Rx scatterers are distributed in the x-y plane and $\kappa_r^{(S)}$ controls the spread of Rx scatterers around the mean $\mu_r^{(S)}$.

The Tx and Rx elevation angles are characterized by the cosine pdf in (3) as

$$f\left(\theta_t^{(S)}\right) = \begin{cases} \dfrac{\pi}{4|\theta_{tm}|}\cos\left(\dfrac{\pi}{2}\dfrac{\theta_t^{(S)}}{\theta_{tm}}\right), & \left|\theta_t^{(S)}\right| \le |\theta_{tm}| \le \dfrac{\pi}{2}, \\ 0, & \text{otherwise}, \end{cases}$$
$$f\left(\theta_r^{(S)}\right) = \begin{cases} \dfrac{\pi}{4|\theta_{rm}|}\cos\left(\dfrac{\pi}{2}\dfrac{\theta_r^{(S)}}{\theta_{rm}}\right), & \left|\theta_r^{(S)}\right| \le |\theta_{rm}| \le \dfrac{\pi}{2}, \\ 0, & \text{otherwise}, \end{cases} \tag{45}$$

where θ_{tm} is the maximum elevation angle for the Tx scatterers and θ_{rm} is the maximum elevation angle for the Rx scatterers.

The pdfs used to characterize the radii R_t and R_r are given by

$$f(R_t) = \frac{3R_t^2}{R_{t2}^3 - R_{t1}^3} \quad R_{t1} \le R_t \le R_{t2},$$
$$f(R_r) = \frac{3R_r^2}{R_{r2}^3 - R_{r1}^3} \quad R_{r1} \le R_r \le R_{r2}. \tag{46}$$

The pdf of phase-offset random variables $\phi_m^{(pol)}$, $\phi_{ab}^{(m)}$, $\phi_{ab}^{(n)}$, and $\phi_{ab}^{(m,n)}$ ($a \in \{p, \tilde{p}\}$ and $b \in \{q, \tilde{q}\}$) is given by a uniform distribution on the interval $[-\pi, \pi)$. Using these distributions, the TFCFs $\rho^{\mathrm{SBT}}(\Delta t, \Delta f)$, $\rho^{\mathrm{SBR}}(\Delta t, \Delta f)$, $\rho^{\mathrm{DB}}(\Delta t, \Delta f)$, and $\rho^{\mathrm{LOS}}(\Delta t, \Delta f)$ of the time-variant transfer functions for the corresponding SBT, SBR, DB and LOS components are derived below.

Using these pdfs it is possible to formulate the TFCFs for each of the bounce path components. The TFCFs along the SBT path are given by

$$\rho_{ab}^{\mathrm{SBT}}\left(\Delta_t, \Delta_f\right) = \frac{\eta_{t,pq}A_m^2}{K+1} I_{ab}^{\mathrm{SBT}}\left(\Delta_t, \Delta_f\right), \tag{47}$$

where $I_{ab}^{\mathrm{SBT}}(\Delta_t, \Delta_f)$ is defined as

$$\begin{aligned} I_{ab}^{\mathrm{SBT}}&\left(\Delta_t, \Delta_f\right) \\ &= \frac{1}{8|\theta_{tm}|I_0\left(\kappa_t^{(s)}\right)} \int_{R_{t1}}^{R_{t2}} \int_{-\theta_{tm}}^{\theta_{tm}} \int_{-\pi}^{\pi} \left(1 - \frac{\gamma}{2}\frac{R_t}{D}\right)^2 \\ &\quad \times \exp\left[-j\frac{2\pi}{c}\Delta_f\left(\epsilon_{p,m} + \epsilon_{m,q}\right)\right] \frac{3R_t^2}{R_{t2}^3 - R_{t1}^3} \\ &\quad \times \cos\left(\frac{\pi}{2}\frac{\theta_t^{(s)}}{\theta_{tm}}\right) \exp\left[\kappa_t^{(s)}\cos\left(\phi_t^{(s)} - \mu_t^{(s)}\right)\right] \\ &\quad \times \exp\left[j2\pi\Delta_t f_{t\max}\cos\left(\phi_t^{(s)} - \phi_{vt}\right)\cos\theta_t^{(s)}\cos\theta_{vt}\right] \\ &\quad \times \exp\left(j2\pi\Delta_t f_{t\max}\sin\theta_t^{(s)}\sin\theta_{vt}\right) \\ &\quad \times \exp\left[j2\pi\Delta_t f_{r\max}\cos\left(\phi_r^{(s)} - \phi_{vr}\right)\cos\left(\theta_r^{(s)}\right)\cos\theta_{vr}\right] \\ &\quad \times \exp\left(j2\pi\Delta_t f_{r\max}\sin\theta_r^{(s)}\sin\theta_{vr}\right) \\ &\quad \times \exp\left[-8\left(\frac{\pi\sigma_h\sin\theta_t^{(i)}}{\lambda_c}\right)^2\right] I_0\left[8\left(\frac{\pi\sigma_h\sin\theta_t^{(i)}}{\lambda_c}\right)^2\right] \\ &\quad \times E\left[\sqrt{\frac{1}{\mathrm{CPR}_{qp,\tilde{q}\tilde{p}}}}\right]\left[\sqrt{G_a^{(v)}\left(\phi_t^{(s)}, \theta_t^{(s)}\right)} \quad \sqrt{G_a^{(h)}\left(\phi_t^{(s)}, \theta_t^{(s)}\right)}\right] \\ &\quad \times \begin{bmatrix} 1 & E\left[\sqrt{r_{p\tilde{q}}^{(m)}}\right] \\ E\left[\sqrt{r_{\tilde{p}q}^{(m)}}\right] & 1 \end{bmatrix} \begin{bmatrix} \sqrt{G_b^{(v)}\left(\phi_r^{(s)}, \theta_r^{(s)}\right)} \\ \sqrt{G_b^{(h)}\left(\phi_r^{(s)}, \theta_r^{(s)}\right)} \end{bmatrix} \\ &\quad \times d\phi_t^{(s)} d\theta_t^{(s)} dR_t. \end{aligned} \tag{48}$$

$E[\sqrt{r_{p\tilde{q}}^{(m)}}]$ and $E[\sqrt{r_{\tilde{p}q}^{(m)}}]$ represent the expectations of the random variables $\sqrt{r_{p\tilde{q}}^{(m)}}$ and $\sqrt{r_{\tilde{p}q}^{(m)}}$, respectively, over the interval $[-20\,\mathrm{dB}, 20\,\mathrm{dB}]$. They are calculated using the pdf of the normal XPD model in (16). $E[\sqrt{\mathrm{CPR}_{qp,\tilde{q}\tilde{p}}}]$ denotes the expectation of random variable of copolar ratio over the interval $[0, 6\,\mathrm{dB}]$.

At the Rx, the azimuth angle $\phi_r^{(s)}$ and elevation angle $\theta_r^{(s)}$ induced by the scatterer $S_t^{(m)}$ are approximated as

$$\phi_r^{(s)} \approx \frac{3\pi}{2} + \frac{R_t}{D}\sin\phi_t^{(s)},$$
$$\theta_r^{(s)} \approx \frac{R_t}{D}\theta_t^{(s)} + \frac{\Delta_z}{D}. \tag{49}$$

The angle of incidence $\theta_t^{(i)}$ with the surface of Tx scatterer can be determined by using trigonometric identities in the triangle $O_t - S_t^{(m)} - O_r$ as follows:

$$\theta_t^{(i)} \approx \frac{1}{2}\arccos\left(\frac{R_t^2 + d_{m,r}^2 - D^2}{2R_t d_{m,r}}\right), \tag{50}$$

where $d_{m,r}$ is given by

$$d_{m,r}^2 = \left(\Delta_x - R_t\cos\theta_t^{(s)}\cos\phi_t^{(s)}\right)^2 + \left(\Delta_y - R_t\cos\theta_t^{(s)}\sin\phi_t^{(s)}\right)^2 + \left(\Delta_z - R_t\sin\theta_t^{(s)}\right)^2. \tag{51}$$

The TFCFs along the SBR path are given by

$$\rho_{ab}^{\mathrm{SBR}}\left(\Delta_t,\Delta_f\right) = \frac{\eta_{r,ab}A_m^2}{K+1} I_{ab}^{\mathrm{SBR}}\left(\Delta_t,\Delta_f\right), \tag{52}$$

where $I_{ab}^{\mathrm{SBR}}(\Delta_t,\Delta_f)$ is defined as

$$\begin{aligned}
&I_{ab}^{\mathrm{SBR}}\left(\Delta_t,\Delta_f\right)\\
&= \frac{1}{8|\theta_{rm}|I_0\left(\kappa_r^{(s)}\right)}\int_{R_{r1}}^{R_{r2}}\int_{-\theta_{rm}}^{\theta_{rm}}\int_{-\pi}^{\pi}\left(1-\frac{\gamma}{2}\frac{R_r}{D_2}\right)^2\\
&\quad\times\exp\left[-j\frac{2\pi}{c}\Delta_f\left(\epsilon_{p,n}+\epsilon_{n,q}\right)\right]\frac{3R_r^2}{R_{r2}^3-R_{r1}^3}\\
&\quad\times\cos\left(\frac{\pi}{2}\frac{\theta_r^{(s)}}{\theta_{rm}}\right)\exp\left[\kappa_r^{(s)}\cos\left(\phi_r^{(s)}-\mu_r^{(s)}\right)\right]\\
&\quad\times\exp\left[j2\pi\Delta_t f_{t\max}\cos\left(\phi_t^{(s)}-\phi_{vt}\right)\cos\theta_t^{(s)}\cos\theta_{vt}\right]\\
&\quad\times\exp\left(j2\pi\Delta_t f_{t\max}\sin\theta_t^{(s)}\sin\theta_{vt}\right)\\
&\quad\times\exp\left[j2\pi\Delta_t f_{r\max}\cos\left(\phi_r^{(s)}-\phi_{vr}\right)\cos\theta_r^{(s)}\cos\theta_{vr}\right]\\
&\quad\times\exp\left(j2\pi\Delta_t f_{r\max}\sin\theta_r^{(s)}\sin\theta_{vr}\right)\\
&\quad\times\exp\left[-8\left(\frac{\pi\sigma_h\sin\theta_r^{(i)}}{\lambda_c}\right)^2\right]I_0\left[8\left(\frac{\pi\sigma_h\sin\theta_r^{(i)}}{\lambda_c}\right)^2\right]\\
&\quad\times E\left[\sqrt{\frac{1}{CPR_{qp,\tilde{q}\tilde{p}}}}\right]\left[\sqrt{G_a^{(v)}\left(\phi_t^{(s)},\theta_t^{(s)}\right)}\ \ \sqrt{G_a^{(h)}\left(\phi_t^{(s)},\theta_t^{(s)}\right)}\right]\\
&\quad\times\begin{bmatrix}1 & E\left[\sqrt{r_{p\tilde{q}}^{(n)}}\right]\\ E\left[\sqrt{r_{\tilde{p}q}^{(n)}}\right] & 1\end{bmatrix}\begin{bmatrix}\sqrt{G_b^{(v)}\left(\phi_r^{(s)},\theta_r^{(s)}\right)}\\ \sqrt{G_b^{(h)}\left(\phi_r^{(s)},\theta_r^{(s)}\right)}\end{bmatrix}\\
&\quad\times d\phi_r^{(s)}d\theta_r^{(s)}dR_r,
\end{aligned} \tag{53}$$

where $E[\sqrt{r_{p\tilde{q}}^{(n)}}]$ and $E[\sqrt{r_{\tilde{p}q}^{(n)}}]$ represent the expectations of the random variables $\sqrt{r_{p\tilde{q}}^{(n)}}$ and $\sqrt{r_{\tilde{p}q}^{(n)}}$, respectively. They are calculated over the interval $[-20\,\mathrm{dB}, 20\,\mathrm{dB}]$ using the pdf of the normal XPD model in (16).

At the Tx, the azimuth angle $\phi_t^{(s)}$ and elevation angle $\theta_t^{(s)}$ induced by the scatterer $S_r^{(n)}$ are approximated as

$$\phi_t^{(s)} \approx \frac{R_r}{D}\sin\phi_r^{(s)},$$
$$\theta_t^{(s)} \approx \frac{R_r}{D}\theta_r^{(s)} - \frac{\Delta_z}{D}. \tag{54}$$

The angle of incidence $\theta_r^{(i)}$ with the surface of Rx scatterer can be determined by using trigonometric identities in the triangle $O_t - S_r^{(n)} - O_r$ as follows:

$$\theta_r^{(i)} \approx \frac{1}{2}\arccos\left(\frac{R_r^2 + d_{t,n}^2 - D^2}{2R_r d_{t,n}}\right), \tag{55}$$

where $d_{t,n}$ is given by

$$d_{t,n}^2 = \left(\Delta_x + R_r\cos\theta_r^{(s)}\cos\phi_r^{(s)}\right)^2 + \left(\Delta_y + R_r\cos\theta_r^{(s)}\sin\phi_r^{(s)}\right)^2 + \left(\Delta_z + R_r\sin\theta_r^{(s)}\right)^2. \tag{56}$$

The TFCFs along the DB path are given by

$$\rho_{ab}^{\mathrm{DB}}\left(\Delta_t,\Delta_f\right) = \frac{\eta_{tr,ab}A_m^2}{K+1} I_{ab}^{\mathrm{DB}}\left(\Delta_t,\Delta_f\right), \tag{57}$$

where $I_{ab}^{\mathrm{DB}}(\Delta_t,\Delta_f)$ is defined as

$$
\begin{aligned}
I_{ab}^{\mathrm{DB}}&\left(\Delta_t,\Delta_f\right)\\
&=\frac{1}{64|\theta_{tm}||\theta_{rm}|I_0\left(\kappa_t^{(s)}\right)I_0\left(\kappa_r^{(s)}\right)}\\
&\quad\times\int_{R_{t1}}^{R_{t2}}\int_{R_{r1}}^{R_{r2}}\int_{-\theta_{tm}}^{\theta_{tm}}\int_{-\theta_{rm}}^{\theta_{rm}}\int_{-\pi}^{\pi}\int_{-\pi}^{\pi}\left(1-\frac{\gamma}{2}\frac{R_r+R_t}{D}\right)^2\\
&\quad\times\exp\left[-j\frac{2\pi}{c}\Delta_f\left(\epsilon_{p,m}+\epsilon_{m,n}+\epsilon_{n,q}\right)\right]\\
&\quad\times\frac{3R_r^2}{R_{r2}^3-R_{r1}^3}\frac{3R_t^2}{R_{t2}^3-R_{t1}^3}\cos\left(\frac{\pi}{2}\frac{\theta_t^{(s)}}{\theta_{tm}}\right)\cos\left(\frac{\pi}{2}\frac{\theta_r^{(s)}}{\theta_{rm}}\right)\\
&\quad\times\exp\left[\kappa_t^{(s)}\cos\left(\phi_t^{(s)}-\mu_t^{(s)}\right)\right]\exp\left[\kappa_r^{(s)}\cos\left(\phi_r^{(s)}-\mu_r^{(s)}\right)\right]\\
&\quad\times\exp\left[j2\pi\Delta_t f_{t\max}\cos\left(\phi_t^{(s)}-\phi_{vt}\right)\cos\theta_t^{(s)}\cos\theta_{vt}\right]\\
&\quad\times\exp\left(j2\pi\Delta_t f_{t\max}\sin\theta_t^{(s)}\sin\theta_{vt}\right)\\
&\quad\times\exp\left[j2\pi\Delta_t f_{r\max}\cos\left(\phi_r^{(s)}-\phi_{vr}\right)\cos\theta_r^{(s)}\cos\theta_{vr}\right]\\
&\quad\times\exp\left(j2\pi\Delta_t f_{r\max}\sin\theta_r^{(s)}\sin\theta_{vr}\right)\\
&\quad\times\exp\left[-8\left(\frac{\pi\sigma_h\sin\theta_t^{(i)}}{\lambda_c}\right)^2\right]I_0\left[8\left(\frac{\pi\sigma_h\sin\theta_t^{(i)}}{\lambda_c}\right)^2\right]\\
&\quad\times\exp\left[-8\left(\frac{\pi\sigma_h\sin\theta_r^{(i)}}{\lambda_c}\right)^2\right]I_0\left[8\left(\frac{\pi\sigma_h\sin\theta_r^{(i)}}{\lambda_c}\right)^2\right]\\
&\quad\times E\left[\sqrt{\frac{1}{\mathrm{CPR}_{qp,\tilde{q}\tilde{p}}}}\right]\left[\sqrt{G_a^{(v)}\left(\phi_t^{(s)},\theta_t^{(s)}\right)}\quad\sqrt{G_a^{(h)}\left(\phi_t^{(s)},\theta_t^{(s)}\right)}\right]\\
&\quad\times\begin{bmatrix}1 & E\left[\sqrt{r_{p\tilde{q}}^{(m)}}\right]\\ E\left[\sqrt{r_{\tilde{p}q}^{(m)}}\right] & 1\end{bmatrix}\begin{bmatrix}1 & E\left[\sqrt{r_{p\tilde{q}}^{(n)}}\right]\\ E\left[\sqrt{r_{\tilde{p}q}^{(n)}}\right] & 1\end{bmatrix}\\
&\quad\times\begin{bmatrix}\sqrt{G_b^{(v)}\left(\phi_r^{(s)},\theta_r^{(s)}\right)}\\ \sqrt{G_b^{(h)}\left(\phi_r^{(s)},\theta_r^{(s)}\right)}\end{bmatrix}d\phi_r^{(s)}d\phi_t^{(s)}d\theta_r^{(s)}d\theta_t^{(s)}dR_rdR_t.
\end{aligned}
\tag{58}
$$

The TFCFs along the LOS path are written in forms as

$$
\rho_{pq}^{\mathrm{LOS}}\left(\Delta_t,\Delta_f\right)=\frac{A_m^2}{K+1}I_{\mathrm{LOS}}\left(\Delta_t,\Delta_f\right),
\tag{59}
$$

where $I_{\mathrm{LOS}}(\Delta_t,\Delta_f)$ is defined as

$$
\begin{aligned}
I_{\mathrm{LOS}}\left(\Delta_t,\Delta_f\right)&=K\exp\left(-j\frac{2\pi}{c}\Delta_f\epsilon_{pq}\right)\\
&\quad\times\exp\left[j2\pi\Delta_t f_{t\max}\cos\left(\pi-\phi_r^{(\mathrm{LOS})}-\phi_{vt}\right)\sin\theta_{vt}\right]\\
&\quad\times\exp\left[j2\pi\Delta_t f_{r\max}\cos\left(\phi_r^{(\mathrm{LOS})}-\phi_{vr}\right)\sin\theta_{vr}\right].
\end{aligned}
\tag{60}
$$

Table 1: The list of parameters used in the simulation.

Parameter	K	γ	$f_{t\max}$ [Hz]	$f_{r\max}$ [Hz]	σ_h [mm]
Value	0	3	100	100	0.2
Parameter	Δ_x [m]	Δ_y [m]	Δ_z [m]	f_c [GHz]	η_t
Value	1500	0	0	1.0	0.2
Parameter	θ_{vt}	θ_{vr}	ϕ_{vt}	ϕ_{vr}	η_r
Value	pi/4	pi/4	$\pi/4$	$\pi/4$	0.2
Parameter	XPD-μ	XPD-σ	CPR-μ	CPR-σ	η_{tr}
Value	10 dB	6 dB	0 dB	3 dB	0.6
V-V/H-H link					
Parameter	R_{t1} [m]	R_{t2} [m]	R_{r1} [m]	R_{r2} [m]	$\kappa_t^{(s)}$
Value	10	100	10	100	3
Parameter	$\kappa_r^{(s)}$	$\mu_t^{(s)}$	$\mu_r^{(s)}$	θ_{tm} [deg]	θ_{rm} [deg]
Value	3	$\pi/4$	$7\pi/4$	20	20
V-H/H-V link					
Parameter	R_{t1} [m]	R_{t2} [m]	R_{r1} [m]	R_{r2} [m]	$\kappa_t^{(s)}$
Value	10	100	10	100	3
Parameter	$\kappa_r^{(s)}$	$\mu_t^{(s)}$	$\mu_r^{(s)}$	θ_{tm} [deg]	θ_{rm} [deg]
Value	3	$\pi/4$	$7\pi/4$	20	20

Numerical integration methods are used to evaluate these TFCFs in the simulation analysis section.

4. Numerical Results and Analysis

In this section, we present numerical results associated with the analysis of the 2×2 DP-MIMO system. The matched polarization-basis time-frequency correlation functions are evaluated using the models described in Section 3. In the analysis, the propagation paths include LOS, SBT, SBR, and DB bounce paths, where the DB paths predominate over the SBT and SBR paths. The temporal dispersion is on the order of 600 ns, and the Doppler spread is approximately 200 Hz. The mean CP power ratio $\mathrm{CPR}_{qp,\tilde{q}\tilde{p}}$ is set to 0 dB so that the average powers of the V- V link and the H-H link are approximately identical, a condition that we recognize will not always hold in operational channels. Further, we also assume that the von Mises distributions for the azimuth angles and the cosine distributions for the elevation angles are equivalent for both H scatterers (reflecting horizontally polarized waves) and V scatterers (reflecting vertical polarized waves), and that the XPD's probability distribution functions are identical for the H-V and V- H components. As before, these are assumed for expediency. The specific simulation parameters are listed in Table 1. The center frequency is assumed to be 1 GHz.

Figures 5, 6, 7, 8, and 9 provide examples of joint TFCFs that were computed for specific subchannels and bounce path components. $\rho_{pq}^{\mathrm{SBT}}(\Delta_t,\Delta_f)$, $\rho_{pq}^{\mathrm{DB}}(\Delta_t,\Delta_f)$, and $\rho_{pq}(\Delta_t,\Delta_f)$ are shown for the V- V CP components in Figures 5, 6, and 7, respectively. Similarly, $\rho_{\tilde{p}q}^{\mathrm{SBT}}(\Delta_t,\Delta_f)$ and $\rho_{\tilde{p}q}^{\mathrm{DB}}(\Delta_t,\Delta_f)$ are shown in Figures 8, and 9 for the H-V link. The correlations along the Δt axis are driven by the Doppler frequency spread [35] and correlations along the Δf axis are driven by

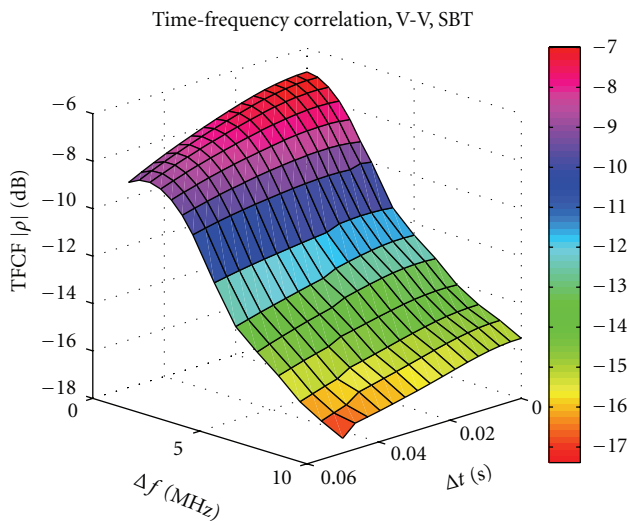

Figure 5: Normalized time-frequency correlation function of V-V link for SBT ray.

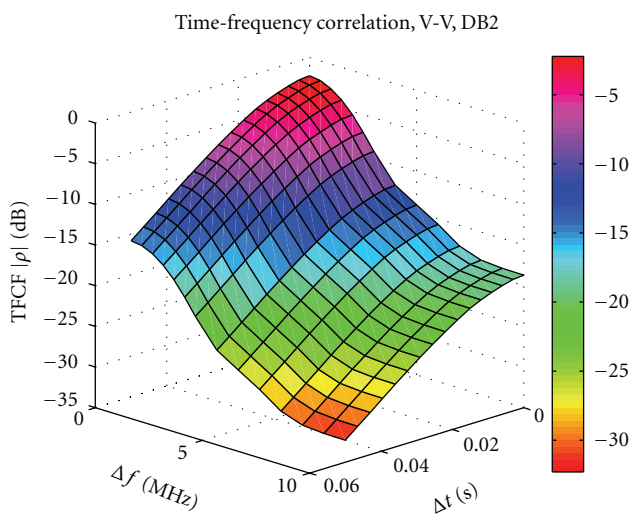

Figure 6: Normalized time frequency correlation function of V-V link for DB ray.

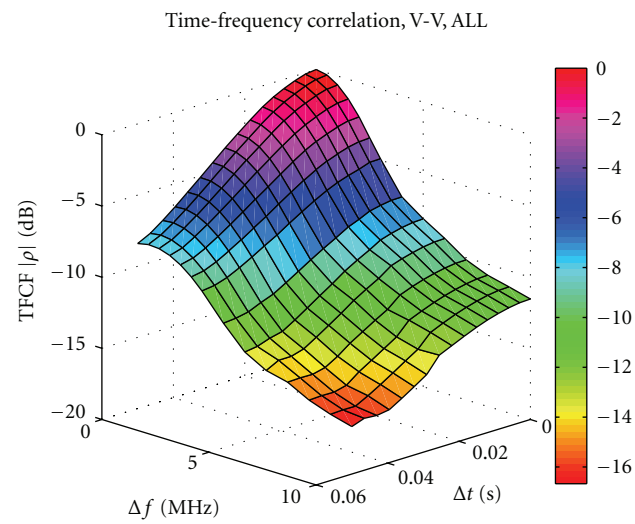

Figure 7: Normalized time frequency correlation function of V-V link for the superposition of SBT, SBR and DB rays.

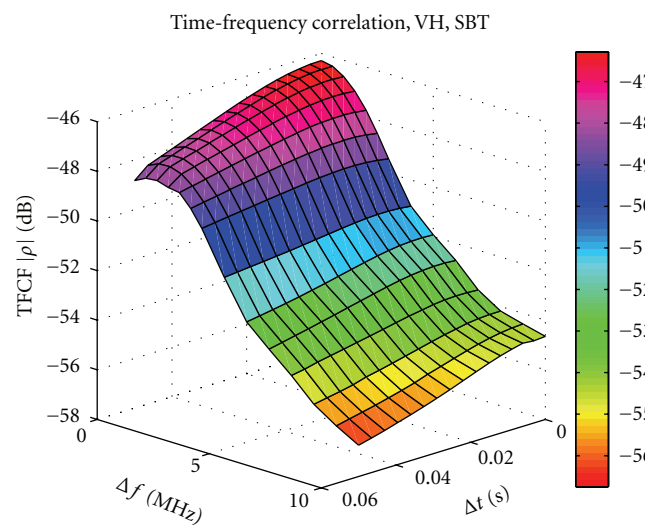

Figure 8: Normalized time-frequency correlation function of V-H link for SBT ray.

the delay spread associated with each component. The results indicate that the TFCFs are not separable into a product of a time correlation function and a frequency correlation function, a conclusion that we anticipated since the scatter locations contribute to both the time dispersion and the Doppler spread. The peak correlation value at $\Delta t = \Delta f = 0$ in each plot is determined by the relative power of the paths being considered. The physical model parameters that play a role in generating temporal and Doppler spread include the radii R_{r1}, R_{r2}, R_{t1}, and R_{t2} associated with the Rx and Tx spheres of scatterers, the maximum elevation angles θ_{rm} and θ_{tm}, the mean value of the azimuth angles $\mu_r^{(s)}$ and $\mu_t^{(s)}$, the spread factor of scatterers $\kappa_r^{(s)}$ and $\kappa_t^{(s)}$, the angles defining the direction of the velocity, θ_{vr}, ϕ_{vr}, θ_{vt}, and ϕ_{vt}, and the maximum Doppler frequencies $f_{r\,\max}$ and $f_{t\,\max}$.

Frequency correlation functions (for a fixed Δt) are driven primarily by the delay profile of the channel. Small delay profiles yield frequency correlation functions that decorrelate at higher frequencies. The DB component will exhibit the lowest decorrelation frequency since this component has the most significant delay spread. In the concentric-sphere based scattering model shown in Figure 1, the maximum delay spread is determined by the maximum distance of signal traveling along the double-bounce path induced by the Tx scatterer or the Rx scatterer. It can be roughly calculated as $(2R_t + 2R_r)/c$, where c is the speed of light. The coherence bandwidth W_c in Hz is given approximately by the inverse proportion of the time delay spread τ_d. The minimum coherence bandwidths versus the radii of the Tx and Rx spheres used in the channel model are estimated and presented in Figures

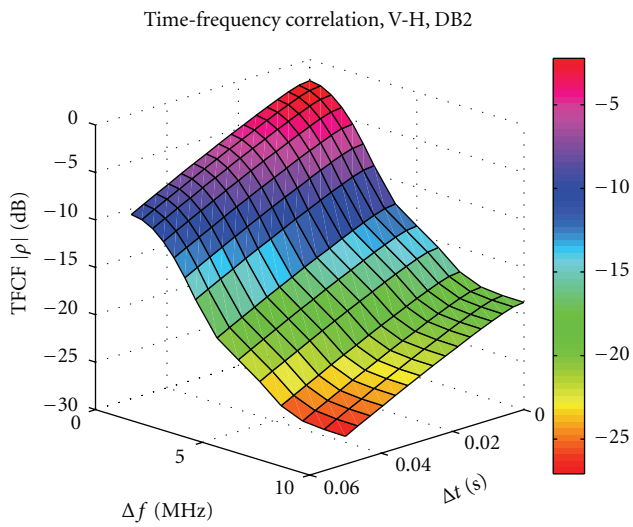

Figure 9: Normalized time-frequency correlation function of V-H link for DB ray.

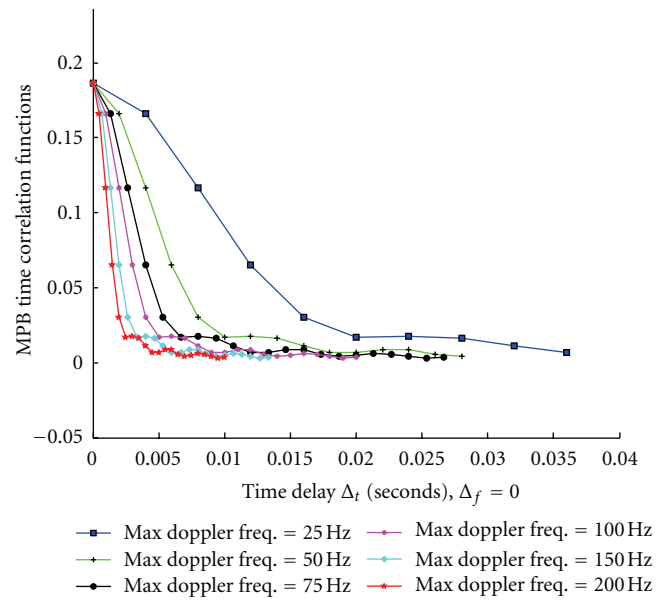

Figure 10: Normalized time-correlation functions varying with the time delay and the maximum Doppler Tx/Rx frequencies for DB ray. The configuration is defined in Table 1 with $\eta_t = \eta_r = \eta_{tr}$=1/3.

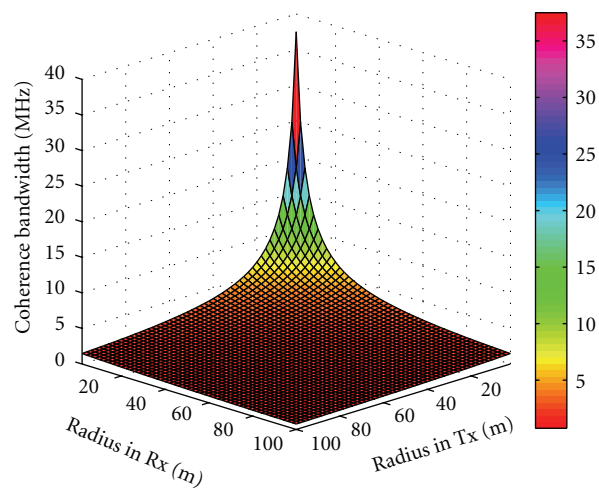

Figure 11: The minimum coherence bandwidth of 2 × 2 DP system varies with upper radii of spheres of Tx and Rx scatterers respectively.

11 and 12. The coherence bandwidth decreases when the radii of the Tx or Rx spheres increase. In Figure 7, if we approximate the coherence bandwidth as the frequency separation over which the magnitude of correlation coefficients is larger than a half of the its maximum at the zero frequency separation, the coherence bandwidth for the test profile used in our analysis is approximately 2.5 MHz.

The time correlation function dependencies on the maximum Doppler frequency are illustrated for the double-bounce ray with $\Delta f = 0$, in Figure 10. Large Doppler frequencies lead to small decorrelation times. We anticipate that the double-bounce components will decorrelate at least as quickly as the single-bounce components due to the fact that the Doppler spread of this component will be greater than or equal to the Doppler spread of the SBT component, a trend that is confirmed in Figures 8 and 9.

The use of non-zero XPD values leads to cross-polarized components (V-H and H-V) with power contributions lower than the CP components (V-V or H-H). Due to the similarity of parameters used to define the co- and crosspolarized channels, the cross-polarized response is approximately related to the CP ones by a scale factor. This result can be observed from cross-polarized parts of TFCFs in Section 3. The normalized correlation values for the SBT and DB components at $\Delta f = \Delta t = 0$ are plotted as a function of the mean XPD value μ for both matched polarization and cross polarization components in Figure 13. The normalized correlation values for the matched polarizations are constant since the correlations and powers are independent of μ. For the crosspolarization components, the normalized correlation is seen to decrease as μ increases, largely due to changes in relative power. At $\mu = 0$, when the scatterers yield the same average power at both matched and cross-polarized components, the normalized correlation is identical for both the matched and cross-polarization links.

5. Conclusion

In this paper, a 3D geometrical propagation model has been proposed for DP-MIMO mobile-to-mobile Rayleigh and Rician fading channels. The parametric channel model incorporates a number of physical parameters to characterize the channel, including antenna patterns, azimuth/elevation angles of arrival and departure, geometrical distribution of scatterers, K-factor, the maximum Doppler frequency, scattering loss factor, crosspolar discrimination, and copolarization power ratio. Using the key parameters of the model,

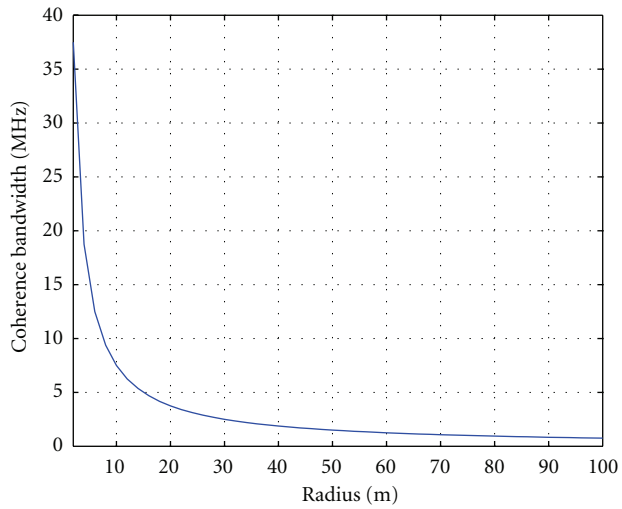

Figure 12: The minimum coherence bandwidth of 2×2 DP system varies with upper radii of spheres of scatterers in both Tx and Rx.

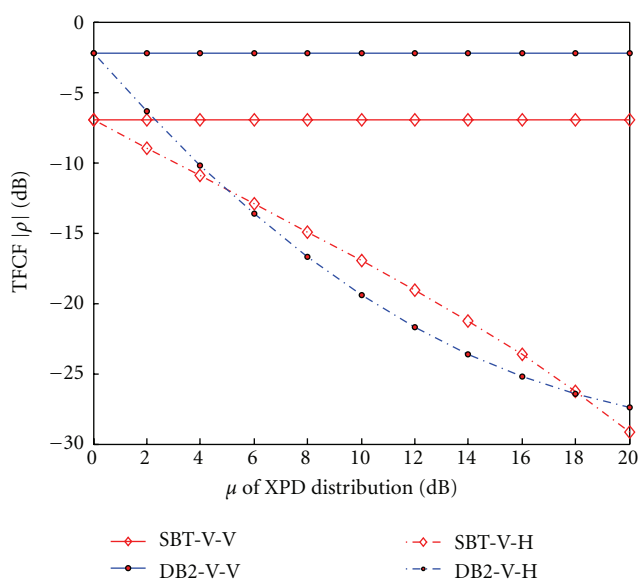

Figure 13: Normalized time-correlation functions of SBT and DB rays vary with the mean XPD μ and the configuration is set up in Table 1.

matched polarization-basis time-frequency correlation functions were formulated and numerically computed for WSSUS 3D non-isotropic scattering environments. The numerical results show that the joint TFCFs are not separable into independent time-correlation and frequency-correlation functions. The normalized TFCFs can be parsed into bounce path components for matched polarization and copolarization links, leading to power-normalized marginal TFCFs for the channel realization. The flexibility of the model enables control of channel parameters to achieve a variety of multipath fading environments to investigate 2×2 DP architectures.

Our intention in future research is to validate the proposed channel model using measurements. A series of experiments are planned to verify and justify our model.

Disclaimer

The views and conclusions contained in this paper are those of the authors and should not be interpreted as representing the official policies, either expressed or implied,of the Office of Naval Research or the U. S. Government.

Acknowledgment

This work was sponsored by the office of Naval Research under grant number N00014-11-1-0607.

References

[1] A. J. Paulraj and T. Kailath, "Increasing capacity in wireless broadcast systems using distributed transmission/directional re-ception (dtdr)," US Patent 5, 345, 599, 1994.

[2] G. J. Foschini and M. J. Gans, "On limits of wireless communications in a fading environment when using multiple antennas," *Wireless Personal Communications*, vol. 6, no. 3, pp. 311–335, 1998.

[3] D. Tse and P. Viswanath, *Fundamentals of Wireless Communication*, Cambridge University Press, 2005.

[4] C. Oestges, V. Erceg, and A. J. Paulraj, "Propagation modeling of MIMO multipolarized fixed wireless channels," *IEEE Transactions on Vehicular Technology*, vol. 53, no. 3, pp. 644–654, 2004.

[5] N. W. Bikhazi, *MIMO communication capacity: antenna coupling and precoding for incoherent detection [Ph.D. thesis]*, CiteSeer, 2006.

[6] P. Soma, D. S. Baum, V. Erceg, R. Krishnamoorthy, and A. J. Paulraj, "Analysis and modeling of Multiple-Input Multiple-Output (MIMO) radio channel based on outdoor measurements conducted at 2.5GHz for fixed BWA applications," in *Proceedings of the IEEE International Conference on Communications (ICC '02)*, vol. 1, pp. 272–276, May 2002.

[7] M. Shafi, M. Zhang, A. L. Moustakas et al., "Polarized MIMO channels in 3-D: models, measurements and mutual information," *IEEE Journal on Selected Areas in Communications*, vol. 24, no. 3, pp. 514–526, 2006.

[8] R. G. Vaughan, "Polarization diversity in mobile communications," *IEEE Transactions on Vehicular Technology*, vol. 39, no. 3, pp. 177–186, 1990.

[9] P. Kyritsi, D. C. Cox, R. A. Valenzuela, and P. W. Wolniansky, "Effect of antenna polarization on the capacity of a multiple element system in an indoor environment," *IEEE Journal on Selected Areas in Communications*, vol. 20, no. 6, pp. 1227–1239, 2002.

[10] T. B. Sorensen, A. O. Nielsen, P. E. Mogensen, M. Tolstrup, and K. Steffensen, "Performance of two-branch polarization antenna diversity in an operational GSM network," in *Proceedings of the 48th IEEE Vehicular Technology Conference (VTC '98)*, vol. 3, pp. 741–746, May 1998.

[11] T. Neubauer and P. C. F. Eggers, "Simultaneous characterization of polarization matrix components in pico cells," in *Proceedings of the IEEE VTS 50th Vehicular Technology Conference (VTC '99)*, vol. 3, pp. 1361–1365, September 1999.

[12] T. G. Pratt, H. Tapse, B. Walkenhorst, and G. Acosta-Marum, "A modified XPC characterization for polarimetric channels," *IEEE Transactions on Vehicular Technology*, vol. 60, no. 7, Article ID 5871726, pp. 2904–2913, 2011.

[13] P. Hoeher, "Statistical discrete-time model for the WSSUS multipath channel," *IEEE Transactions on Vehicular Technology*, vol. 41, no. 4, pp. 461–468, 1992.

[14] E. Chiavaccini and G. M. Vitetta, "GQR models for multipath rayleigh fading channels," *IEEE Journal on Selected Areas in Communications*, vol. 19, no. 6, pp. 1009–1018, 2001.

[15] C. Oestges, B. Clerckx, M. Guillaud, and M. Debbah, "Dual-polarized wireless communications: from propagation models to system performance evaluation," *IEEE Transactions on Wireless Communications*, vol. 7, no. 10, pp. 4019–4031, 2008.

[16] M. Shafi, M. Zhang, P. J. Smith, A. L. Moustakas, and A. F. Molisch, "The impact of elevation angle on MIMO capacity," in *Proceedings of the IEEE International Conference on Communications (ICC '06)*, vol. 9, pp. 4155–4160, July 2006.

[17] T. R. ETSI, "125 996 v. 6.1. 0,universal mobile telecommunications system (umts); spatial channel model for multiple input multiple output (mimo) simulations (3gpp tr 25.996 version 6.1. 0 release 6)," Further study is required to design an adaptive or hybrid MCN structure to improve both the handover effciency and the throughput of cell-edge and cell-boundary users and to resolve the network issues, 2003.

[18] A. G. Zajić and G. L. Stüber, "Three-dimensional modeling and simulation of wideband MIMO mobile-to-mobile channels," *IEEE Transactions on Wireless Communications*, vol. 8, no. 3, pp. 1260–1275, 2009.

[19] M. T. Dao, V. A. Nguyen, Y. T. Im, S. O. Park, and G. Yoon, "3D polarized channel modeling and performance comparison of MIMO antenna configurations with different polarizations," *IEEE Transactions on Antennas and Propagation*, vol. 59, no. 7, pp. 2672–2682, 2011.

[20] R. Wang and D. Cox, "Channel modeling for Ad Hoc mobile wireless networks," in *Proceedings of the 55th Vehicular Technology Conference (VTC '02)*, vol. 1, pp. 21–25, May 2002.

[21] C. S. Patel, G. L. Stüber, and T. G. Pratt, "Simulation of Rayleigh-faded mobile-to-mobile communication channels," *IEEE Transactions on Communications*, vol. 53, no. 11, pp. 1876–1884, 2005.

[22] J. Maurer, T. Fügen, and W. Wiesbeck, "Narrow-band measurement and analysis of the inter-vehicle transmission channel at 5.2 GHz," in *Proceedings of the 55th Vehicular Technology Conference (VTC '02)*, vol. 3, pp. 1274–1278, May 2002.

[23] Y. I. Wu and K. T. Wong, "Polarisation-sensitive geometric modelling of the distribution of direction-of-arrival for uplink multipaths," *IET Microwaves, Antennas and Propagation*, vol. 5, no. 1, pp. 95–101, 2011.

[24] J. D. Kraus and R. J. Marhefka, *Antennas for All Applications*, vol. 1, McGraw-Hill, New York, NY, USA, 2002.

[25] H. L. Van Trees, *Detection, Estimation, and Modulation Theory: Detection, Estimation, and Linear Modulation Theory*, Wiley, 1968.

[26] J. D. Parsons and P. J. D. Parsons, *The Mobile Radio Propagation Channel*, vol. 81, Wiley, 2000.

[27] K. Mammasis, R. W. Stewart, and J. S. Thompson, "Spatial Fading Correlation model using mixtures of von Mises Fisher distributions," *IEEE Transactions on Wireless Communications*, vol. 8, no. 4, pp. 2046–2055, 2009.

[28] E. J. Gumbel, "Applications of the circular normal distribution," *JAMA*, vol. 49, no. 266, pp. 267–297, 1954.

[29] J. D. Parsons and A. M. D. Turkmani, "Characterisation of mobile radio signals. Model description," *IEE Proceedings, Part I*, vol. 138, no. 6, pp. 549–556, 1991.

[30] T. Taga, "Analysis for mean effective gain of mobile antennas in land mobile radio environments," *IEEE Transactions on Vehicular Technology*, vol. 39, no. 2, pp. 117–131, 1990.

[31] P. Kyritsi and D. C. Cox, "Propagation characteristics of horizontally and vertically polarized electric fields in an indoor environment: simple model and results," in *Proceedings of the IEEE 54th Vehicular Technology Conference (VTC '01)*, vol. 3, pp. 1422–1426, October 2001.

[32] L. Boithias and L. J. Libols, *Radio Wave Propagation*, North Oxfordshire Academy, London, UK, 1987.

[33] J. G. Proakis, *Digital Communications*, McGraw-Hill, New York, NY, USA, 2001.

[34] J. M. Wozencraft and I. M. Jacobs, *Principles of Communication Engineering*, vol. 32, Wiley, New York, NY, USA, 1965.

[35] T. S. Rappaport et al., *Wireless Communications: Principles and Practice*, Prentice Hall, Upper Saddle River, NJ, USA, 1996.